EFFECTS OF SLIPPER SURFACE SHAPING AND SWASHPLATE VIBRATION ON SLIPPER-SWASHPLATE INTERFACE PERFORMANCE

A Dissertation

Submitted to the Faculty

of

Purdue University

by

Ashkan A. Darbani

In Partial Fulfillment of the

Requirements for the Degree

of

Master of Science in Mechanical Engineering

May 2019

Purdue University

West Lafayette, Indiana

THE PURDUE UNIVERSITY GRADUATE SCHOOL
STATEMENT OF DISSERTATION APPROVAL

Dr. Andrea Vacca, Chair

School of Mechanical Engineering

Dr. Osman Basaran

School of Chemical Engineering

Dr. Sadegh Dabiri

School of Mechanical Engineering

Approved by:

Dr. Jay Gore

Head of the School Graduate Program

To Mom and Dad and in memory of my beloved sister, Bahar.

TABLE OF CONTENTS

Page

LIST OF TABLES

LIST OF FIGURES

Figure Page

SYMBOLS

Symbol	Description	Units
A	Area	$[m2]$
Ak	Piston area	$[m2]$
ak	Piston acceleration	$[m/s2]$
cp	Heat capacitance	$[J/kg{\cdot}K]$
ddG	Slipper orifice diameter	[m]
$dinG$	Inner pocket diameter	[m]
dK	Piston diameter	[m]
$doutG$	Outer pocket diameter	[m]
E	Elastic modulus	[Pa]
F	Force	$[N]$
FDK	Displacement chamber pressure force	[N]
Ffz	Slipper fluid force	[N]
FHD	Slipper hold down force	[N]
FSK	Piston ball joint force	[N]
FTG	Slipper viscous friction force	[N]
$F\omega G$	Centrifugal force	[N]
g_1, g_2, g_3	Slipper control points	[−]
I	Mass moment of inertia	$[kg{\cdot}m2]$
K	Fluid bulk modulus	$[Pa]$
lG	Distance between slipper socket center and gap	[m]
lSG	Distance between slipper socket center and COG	[m]
mK	Slipper mass	[kg]
mK	Piston / slipper assembly mass	[kg]
M	Moment	$[N{\cdot}m]$
$Mvisc$	Fluid viscous shear moment about slipper socket center	$[N{\cdot}m]$
Mf, MfG	Fluid net pressure moment about slipper socket center	$[N{\cdot}m]$
Mz	Swash plate moment about z-axis	$[N{\cdot}m]$
$M\omega G$	Centrifugal moment	$[N{\cdot}m]$
n	Rotational speed	$[rpm]$
p	Pressure	$[Pa]$
P	Power	[W]
pDC	Displacement chamber pressure	[Pa]
pG	Slipper pocket pressure	[Pa]
Δp	Pressure differential	$[bar]$
q	Heat flux	$[W/m2]$
Q	Volumetric flow rate	$[m3/s]$
Qs	Loss flow rate	$[m3/s]$
Qse	Loss flow through all lubricating interfaces	$[m3/s]$
QSG	Loss flow through slipper orifice	$[m3/s]$
Qsi	Internal volumetric loss flow	$[m3/s]$
Rb	Cylinder block pitch radius	$[m]$
rG	Slipper ellipsoid radius	[m]
$rinG$	Inner pocket radius	[m]
$routG$	Outer pocket radius	[m]
$rsock$	Slipper socket radius	$[m]$
sK	Piston displacement	$[m]$
t	Time	$[s]$
T	Temperature	[°C]
u	Deformation	[m]
v	Velocity	[m/s]
V	Volume	$[m3]$
Vi	Displacement chamber volume	$[m3]$
vK	Piston velocity	$[m/s]$
vxG,vyG	Slipper velocity	$[m/s]$
vG,yG,zG	Slipper local Cartesian coordinates	[−]
xS,yS,zS	Swashplate global coordinates	[−]
zK	Number of pistons	[−]
$\underline{x}$	Design vector	[−]
αD	Orifice coefficient of discharge	[−]
αT	Coefficient of linear thermal expansion	$[m/m°C]$
β	Swash plate angle	[°]
η	Efficiency	[−]
λ	Thermal conductivity	$[W/m{\cdot}K]$
μ	Fluid dynamic viscosity	[Pa·s]
ν	Poisson ratio	[−]
ρ	Oil density	$[kg/m3]$
σ	Stress tensor	[Pa]
τ	Shear stress	[Pa]
φ	Shaft angular position	[°]
ω	Angular velocity	$[rad/s]$

ABSTRACT

Darbani, Ashkan A. MS, Purdue University, May 2019. Effects of Slipper Surface Shaping and Swashplate Vibration on Slipper-swashplate Interface Performance . Major Professor: Monika Ivantysynova Professor.

This thesis investigates the effects of swashplate vibration and slipper surface geometry on the performance of the slipper-swashplate interface. The lubricating interfaces within a swashplate type axial piston machine are the most complicated part of the design process. These interfaces are supposed to provide support to the significant loads they experience during operation and to prevent continuous contact of the sliding surfaces. Therefore a proper slipper-swashplate interface design ensures full film lubrication during operation and provides sufficient load support while minimizing viscous and volumetric losses at the same time. The effects of two factors on the performance of the slipper-swashplate are examined during this work; swashplate vibration and slipper surface micro-geometry. An already existing model of the slipper-swashplate interface was used to carry out the results for this work however some modifications were made to the model to suit the needs of this research. Swashplate vibration is a phenomenon that has not been implemented in the model before, therefore its effects on the performance of the interface were analyzed. Thickness of the fluid film in the lubricating regime corresponds with its performance and is directly affected by the micro-geometry of the sliding interfaces. Therefore the effects of slipper surface micro-geometry is crucial to study in order to find the optimal slipper-swashplate interface design.

1. INTRODUCTION

1.1 Background

Axial piston machines of swashplate type are found in many application in different industries such as agriculture, construction, and aerospace. Reasons for their popularity are their high power density delivery and their capability to continuously vary the effective displacement volume at a high rate. The major parts that build an axial piston machine of swashplate type are the following; the outer case which houses the hydraulic fluid and the remaining components, the end case with its channels to connect the input and output ports to the displacement chambers, a control system, in case of a variable displacement design, is used to vary the inclination angle of the swashplate which in return changes the effective displacement of fluid volume, and finally the rotating kit which is the heart of the machine (fig. 1).

The rotating kit in an axial piston machine of swashplate type consists of three major components; cylinder block, valve plate, and piston-slipper assemblies. The cylinder block encloses the pistons in its bores while being bounded by the valve plate from the end case side and by the slippers and swashplate at the other end. The cylinder block is mounted on the shaft through a spline and with its rotation, the piston-slipper assemblies also rotate. Due to the inclination of the swashplate, the volume of displacement chamber shrinks after suction stroke and an increase in pressure is resulted in displacement chamber. The pressure inside the displacement chamber can typically rise to 40 MPa which exerts forces onto the valve plate and pistons. The forces exerted onto the pistons need to be carried to the swashplate and to the case through the slippers. This is where a proper slipper-swashplate interface design is essential for proper operation of axial piston machines. The three lubricating interfaces in an axial piston machine need to make sure that solid body contact is minimized

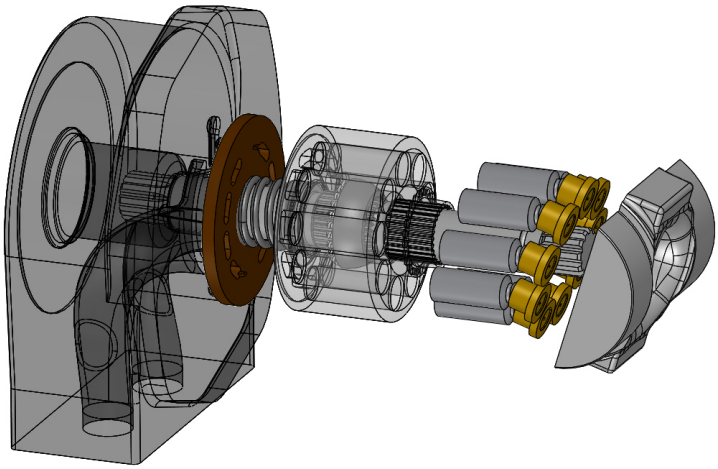

Fig. 1.1.: Axial piston machine of swashplate type with main parts separated

and to seal high pressure fluid from the case as much as possible. There is a trade off between the two fundamental roles of these interfaces; in order to prevent solid body contact, fluid film thickness needs to be higher than the asperities of the two solid bodies, which in return could potentially increase the leakage. Therefore a highly efficient interface design will provide just enough film thickness to provide full film lubrication, but not too much to increase the leakage. This process is not straight forward since these requirements will vary between each different operating condition depending on pressure, speed, and displacement.

A lot of effort is put into modeling these lubricating interfaces as they are the most complex part of the design process. The core of lubrication is a result of Osborne Reynolds' work in 1886. By combining Navier-stokes and continuity equation, he was able to derive a relationship between film thickness and pressure generation in sliding interfaces, called the Reynolds lubrication equation. There are two sources of pressure generation in a lubricating interface, hydrostatic and hydrodynamic. Hydro-

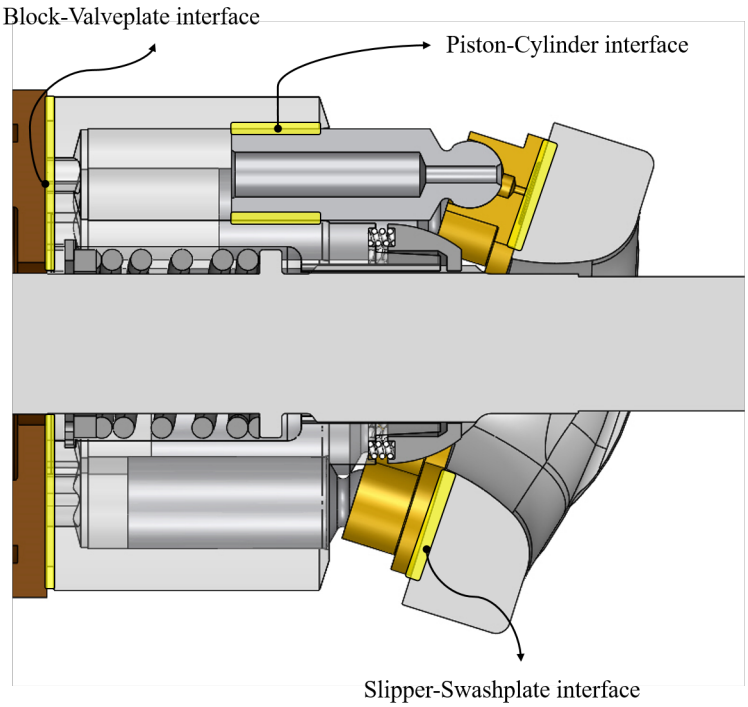

Fig. 1.2.: Lubricating interfaces of the axial piston machine

static pressure generation is straight forward as it uses an external source of pressure to feed into the lubricating interface. In the case slipper-swashplate interface, displacement chamber pressure is directed through an orifice through the piston to the slipper pocket. Acting normal to the slipper pocket, this hydrostatic pressure changes with the load making it an adaptive design which is well needed. A failure to properly size the pocket of a slipper can cause it be either under-balanced or over-balanced. An under-balanced design means that the slipper won't lift off enough to avoid solid body contact and an over-balanced design means that slipper lifts off too much that the leakage to the case increases which in return decreases the efficiency of the interface. The hydrodynamic aspect of pressure generation however, is more complex. Hydrodynamic pressure generations is related to multiple factors. Thin film properties such as viscosity and density play a role in the determining the ability of the working fluid to transmit loads. Due to the film thickness being thin, its temperature can easily

change based on the bounding surface temperatures. Since viscosity of hydraulic oil is very sensitive to thermal changes, the hydraulic oil can potentially lose its load carrying capabilities if it gets too hot. Changes in the fluid's density can also affect the pressure generation through local expansion and density wedge. Another factor that impacts hydrodynamic pressure generation is the deformation of the bounding bodies due to the large pressures of the fluid film and thermal stresses. These elastic deformations will occur wherever pressure is high enough and will cause an alteration to the fluid film thickness which in return will change the pressure generation. The velocity of bounding surfaces play a great role in the amount of hydrodynamic pressure generation as well. Since in the hydrostatic case it was adaptively generated based on the displacement chamber pressure (load), for the hydrodynamic case also it can be adaptively generated based on speed of the pump. This work will mainly focus on the details of the slipper-swashplate interface in an axial piston machine. A fully coupled model previously developed by Schenk (2014) is used as the basis of the research, although alterations are made to the model to adjust to the needs of the research.

1.2 Research Objective

This work is conducted to discover the effects of swashplate vibration on the slipper-swashplate interface performance. Swashplate vibration is a phenomenon that exists in axial piston machines of swashplate type and its effects were missing in the model of the pump. Therefore effort was made to implement the effects of this factor into the model and analyze slipper-swashplate behavior.

This work also focuses on a very important slipper design parameter that has been previously looked at by other researchers Beale (2017) and Schenk (2014). Slipper surface geometry directly affects the Reynolds equation calculation which in turn decides the pressure field in the fluid. This work gives a more thorough and clear

conclusion about the effects of the slipper surface geometry on the performance of the slipper-swashplate interface.

1.3 State of the Art

This section includes previous notable research work about three topics related to this thesis; development of lubrication models, vibration in axial piston machines, and surface shaping of lubricating surfaces. There has been an extensive amount of research conducted into developing models to predict the behavior of fluid film in lubricating interfaces and experimental work alongside to support the models. Starting in 1960s, assuming only hydrostatic operation, Shute and Turnball (1958) measured film thickness under the slipper with analytical prediction model to go along with it. Moreover, they were able to get experimental results for different operating conditions(1964) using different working fluids (1962). One of their works, gave insight to power loss prediction based on slipper pad area and operating condition which was useful in slipper design (1962). One of the more critical pieces of research was done by Hooke and Kakoullis in the 1980s (1978, 1983), which stated that a fully hydrostatic slipper design won't be functional and hydrodynamic pressure generation, in other words a non-flat slipper profile, is needed for proper operation. Iboshi and Yamaguchi (1982, 1983), similarly came up with analytical models and set up their experimental work to measure film thickness as a method to validate their theoretical models. Hooke and Li (1988) started using a finite difference method to solve for the Reynolds equation which enabled use of non-flat surface profiles. With added capability to the models, more experimental work was been worked on. Looking into hydrodynamic pressure generation and characterizing film thickness for centerally loaded slippers, finding the effect of ball-joint on slipper behavior (1989), using water as the working fluid (1991), and effects of clamp ratio and orifice size on slipper behavior were notable research by Hooke and Li in this field. As the computation power was improving, lubricating models were seeing new light as Kazama and Yamaguchi (1993) developed

a mixed-friction model which included the effects of Elastohydrodynamic effects on the asperity only. Further on, Manring (2002) introduced linear deformations on the surfaces and studied their effects in hydrostatic and stationary bearings. With advent of CFD, Bergada (2009) studied the fluid flow behavior in the grooved regions of sealing lands. In 2009, Bergada, Kumar, and Watton were able to give detailed results for pressure and velocity values in the fluid gap of grooved slipper designs. As for the effects of temperature, Wiczorek and Ivantysynova (2000) developed a model that included the temperature results to find the solid body motion which was coupled with Reynolds to find the equilibrium at each shaft rotation. Later on, Ivantysynova and Huang (2003) added pressure deformation (EHL) to the piston-cylinder and block-valveplate interface. Pelosi and Ivantysynova (2012) then extended the effects of EHL to slipper-swashplate interface. He also simulated the thermal effects in the piston-cylinder interface in 2009. Using the thermal model simulations and EHL effects, Schenk (2014) was able to put together a fully coupled fluid-solid-thermal interaction model for the slipper-swashplate interface similar to the work of his contemporaries Pelosi and Zecchi did for piston-cylinder and block-valveplate interfaces respectively.

There were studies done regarding vibration in axial piston machines. Most of these studies were regarded to noise and active vibration systems in axial piston machines. Moreover, studies regarding prognostics also pay attention to the amount of vibration present in the system. In a study by Sudeep, Pandey, and Tandon (2013), they concluded that surface texturing can reduce friction coefficients by 30 percent, and reduce amount of vibration at resonance frequency significantly. A publication by Dong and Dapino (2015) stated that high frequency vibration above 20kHz (ultrasonic) can help reduce friction between two surfaces. They also hinted that surface wear can be reduced at what they call ultrasonic lubrication with a value of 49 percent reduction in wear volume. More recently, Kim (2017) implemented swashplate active control techniques to reduce vibration and noise. His methodology of vibration measurement was studied for this work.

Research on the effects of surface shaping of lubricating surfaces were hinted at previously as done by Hooke and Kakoullis (1981). They stated that moments generated due to centrifugal effects and the slipper-ball-joint friction needed a non-flat slipper design to balance. Similarly, they concluded that for over-clamped slipper designs, a non-flat slipper is needed. Furthermore, Hooke and Kakoullis (1983) studied the effects of non-flatness on film thickness by adding tilt and deviation to the slipper running surface. Hargreaves(1990) studied the effects of surface waviness on the load-carrying ability of rectangular slider bearings and concluded that the performance of the bearings improves with waviness as he measured the pressure to match with his findings. Similarly, Rasheed (1998) studied the effects of surface shaping in cylindrical sliding bearings (journal bearings) and he concluded that load-carrying capacity of these bearings improved with waviness. On a separate study, Yabe (1997) studied the effect of slipper non-flatness due to wear on slipper performance. A few years later, Baker and Ivantysynova (2008), using the model developed by Huang and Ivantysynova (2003), were able to predict 50 percent reduction in power loss by introducing waviness to the block-valveplate interface. They used 15 sinusoidal waves circumferentially on the valve plate sealing land with amplitude of 1 micron. More recently, Chacon and Ivantysynova (2014) were able to confirm the work Baker and Ivantysyn (2008) had done after adding deformation due to thermal effects and broadening the variable bounds. Chacon and Ivantysynova, predicted a 40 percent reduction in power loss and concluded that the amplitude of waves around the valveplate played the most important role. Schenk (2016) and Beale (2017) studied the effect of step design in slipper. Similarly, Wondergem (2018) included in her thesis that different surface shapes including waviness and barrel-like shapes on the piston can benefit the performance of the piston-cylinder interface.

2. THE SLIPPER-SWASHPLATE INTERFACE

In this chapter the kinematics of axial piston machines of swashplate type will be discussed. A detailed section regarding the lubrication operation of the interfaces and an analytical approach to predict the performance of the slipper-swashplate interface will be presented. Furthermore, the details of the numerical model that was used will be discussed.

The majority of the operation of an axial piston machine of swashplate type was discussed in the last chapter. Focusing more on the components related to the slipper-swashplate interface; there are many patented slipper and piston-slipper assembly designs. There are female and male slipper designs, multi-land and single land designs with or without step as shown in Figure 2.1, and many more. The multi-land design has both high pressure and low pressure regions (red (high pressure) and blue (low pressure) in Figure 2.1 a) while single land design with a step has only high pressure (Figure 2.1 b).

However a hydrostatic slipper design provides a better performance due to its adaptive load capability. A hydrostatic slipper design includes a pocket area that shares a pressure close to the displacement chamber pressure and one or multiple sealing lands to seal the high pressure flow in the pocket and to add load capability through hydrodynamic pressure generation. In the more common design of slipper which has one pocket area with one sealing land, the slipper is manufactured with a socket and is swaged around the piston head (Fig. 2.2). This is a female slipper design. One advantage of male slipper design is that it allows for larger swashplate angle since it allows for shorter piston-slipper assembly resulting in less bending moment of the piston.

Basic principle of axial piston machines of swashplate type is as follows; the pistons are encompassed by cylinder bores that are arranged on a circle inside the cylinder

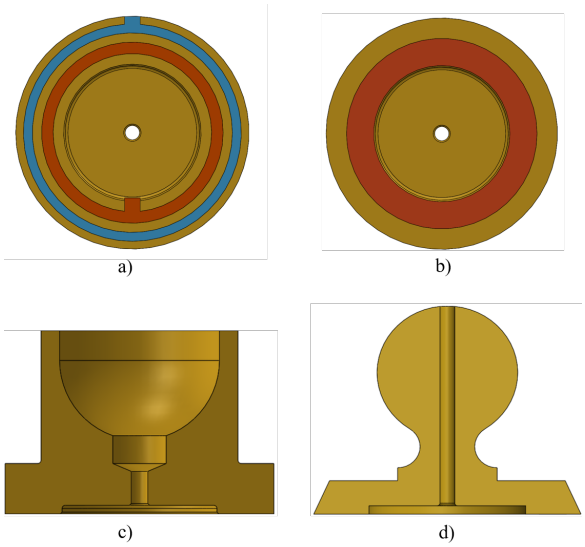

Fig. 2.1.: Different slipper designs; a) multi-land slipper design b) single land with a step c) female design d) male design

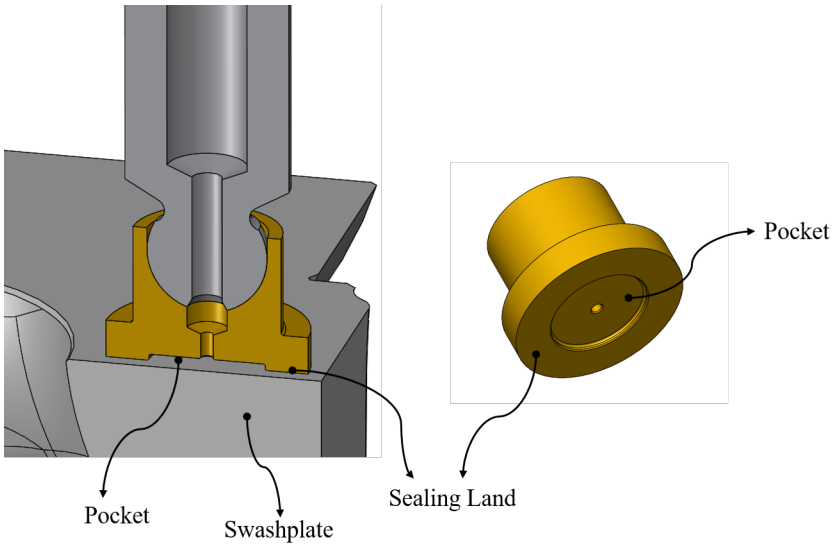

Fig. 2.2.: Single land slipper design with no step

block with a radius of R_b. Due to the inclination of the swashplate, pistons have a linear stroke H_K which depends on the swashplate angle β. The direction of flow can be changed by moving the swashplate over center, without changing the shaft

rotation direction. The flow enters and leaves the displacement chambers through a non-rotating valveplate from suction and pressure ports. Three parts build the mech-

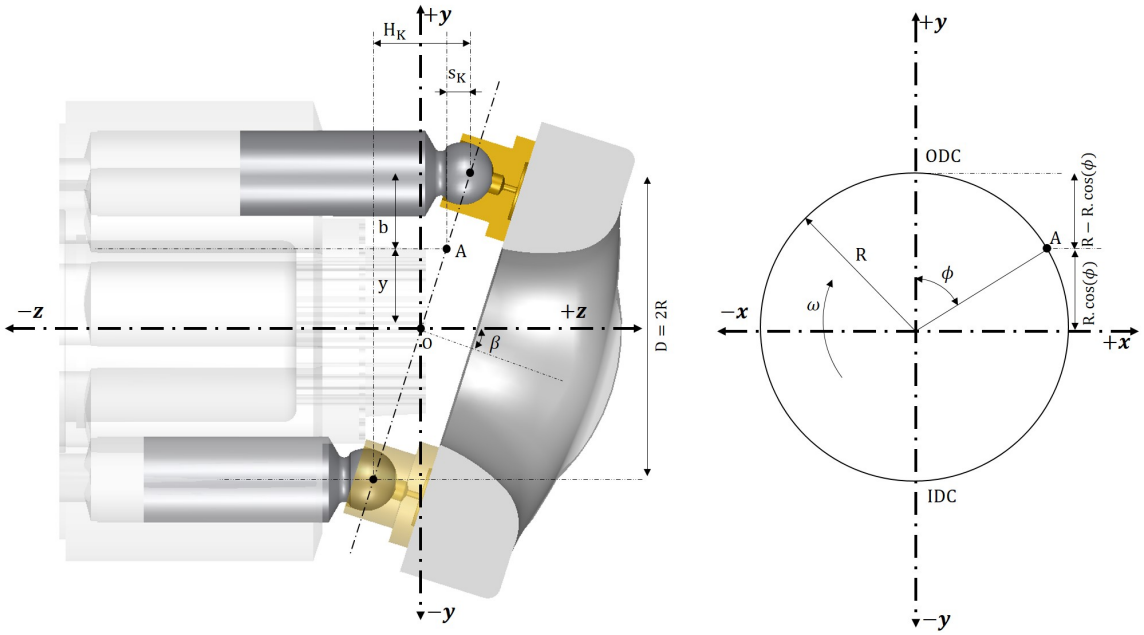

Fig. 2.3.: Axial piston machine schematic

anism of the rotating group; the swashplate and valveplate are connected through the housing and are mostly fixed, the cylinder-block that is connected to the shaft through a spline, and the piston-slipper assembly. The difference between pumps and motors rise from the way torque is transferred; if the torque is transmitted from the shaft to the rotating group, the piston is driven and there will be a pressure difference. This mechanism is regarded as pumping. On the other hand, if the rotating group receives its torque from a pressure difference, it would be regarded as motoring. To derive the kinematics of the axial piston machine, a system is chosen as shown in Figure 2.3 which is only used to obtain kinematics of the pump. the speed of the cylinder block is a constant value ω, the piston is allowed a linear movement along the z direction and also rotation around its own axis. Shaft angle is measured based with reference to initial position OTC (outer dead center), which is the point where

piston is at its full stroke in pumping mode. The piston stroke S_K can be calculated as:

$$S_K = -R \cdot \tan\beta \cdot (1 - \cos\phi) \tag{2.1}$$

With the rotation of the block by $\phi = 180°$, the maximum piston stroke H_K occurs which is:

$$H_K = 2R \cdot \tan\beta \tag{2.2}$$

From equation (2.1), velocity of the piston can be found:

$$v_K = \frac{dS_K}{dt} = \frac{dS_K}{d\phi} \cdot \frac{d\phi}{dt} = -\frac{1}{2} \cdot H_K \cdot \sin\phi \cdot \omega \tag{2.3}$$

And similarly the piston-slipper assembly acceleration can be found to be:

$$a_K = \frac{dv_K}{dt} = \frac{dv_K}{d\phi} \cdot \frac{d\phi}{dt} = -\frac{1}{2} \cdot H_K \cdot \cos\phi \cdot \omega^2 \tag{2.4}$$

Pressure of displacement chamber p_{DC} is ultimately the load for slipper-swashplate interface. It is important to know how the value of p_{DC} is achieved. Using a simple lumped parameter model developed by Wieczorek and Ivantysynova[], the derivation is as follows:

$$\frac{dV_i}{dt} = v_k \cdot A_K \tag{2.5}$$

Where subscript i corresponds to each displacement chamber. Using the definition derived for v_K, pressure can be found by integrating the following equation:

$$\frac{dp_i}{dt} = \frac{K}{V_i}(Q_{ri} - Q_{SK_i} - Q_{SB_i} - Q_{SG_i} - \frac{dV_i}{dt}) \tag{2.6}$$

To analyze slipper-swashplate interface analytically, a global coordinate system is defined just for this interface. This coordinate system is defined at the center of the slipper motion path on swashplate surface, hence it is named (x_S, y_S, z_S). Referring to Figure 2.5, the y-axis is parallel to the surface of swashplate and in a straight line from IDC to ODC, the z-axis is normal to the surface and pointing away, and x-axis can be found using right-hand rule. The shaft rotation angle ϕ is zero at positive

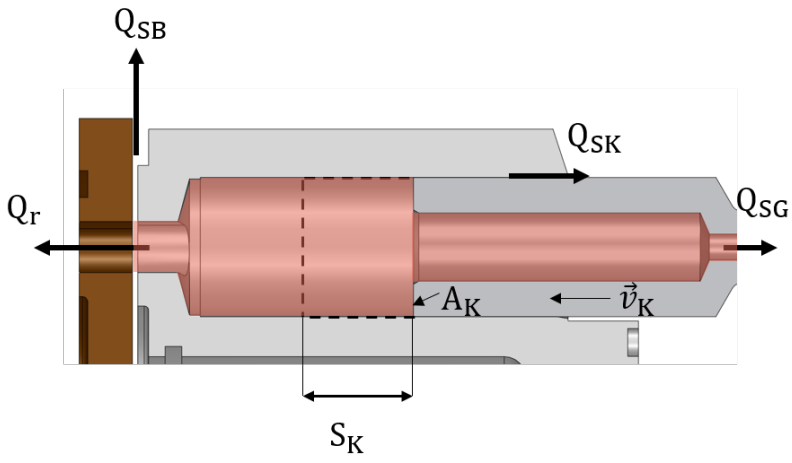

Fig. 2.4.: Flow rates corresponding to pressure build-up in displacement chamber

y-axis (ODC) by convention in pumping mode. Piston centerline stays at a constant radius R_B throughout a revolution. However, when swashplate is not zero, the path of motion of slippers becomes elliptical and the instantaneous radius of a slipper r_G as a function of revolution angle can be found as follows:

$$r_G = \sqrt{(R_B \sin(\phi))^2 + (\frac{R_B}{\cos(\beta)} \cos(\phi))^2} \tag{2.7}$$

Since each slipper goes through the same operation, this work only focuses on analyzing one slipper. In order to predict the performance of the whole unit, the results need to be correctly phase shifted based on the number of pistons and then summed together assuming each slipper shares the same exact geometry. To focus on one slipper, another coordinate system is introduced. This coordinate system has its origin on the center of sealing land surface, with z-axis pointing outward from the swashplate surface, x-axis is tangent to instantaneous slipper velocity, and y-axis can be found based on right-hand rule shown in Figure 2.6. An equivalent cylindrical coordinate system for the slipper is also shown in Figure 2.6 due to the fact that thin film will be discretized based on polar coordinates due to the nature of the thin film looking like a disk, making it simpler to use polar coordinate system. As shown, r and θ will go through all of the discretized thin film for every increment of shaft revolution. With

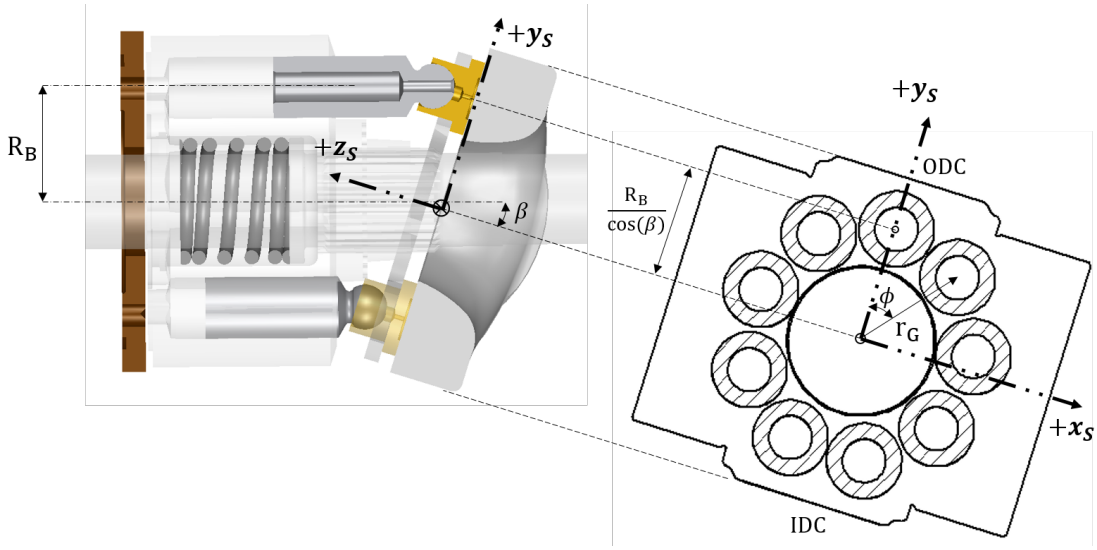

Fig. 2.5.: Swashplate coordinate system (global)

the local coordinate system defined, the complete motion of slipper can be analyzed. The relative rotation of piston around its own axis was examined by Ivantysynova and Lassar [] through a special test rig to measure the friction between piston and cylinder bore. It is assumed that for every full revolution, piston rotates around itself once. It is also assumed that slipper rotates with piston's relative rotation around its own axis. Therefore slipper also rotates around z_G once every revolution. The equation of slipper velocity in polar coordinates is as follows:

$$\begin{aligned} v_{x_G}(r,\theta) &= \omega \cdot c_1 \cdot \cos(c_2) \\ v_{y_G}(r,\theta) &= \omega \cdot c_1 \cdot \sin(c_2) - r \cdot \omega \\ c_1 &= \sqrt{r^2 + {r_G}^2 - 2 \cdot r_G \cdot r \cdot \cos(\pi - \theta)} \\ c_2 &= \frac{\pi}{2} - \cos^{-1}\left(\frac{{c_1}^2 + r^2 - {r_G}^2}{2 \cdot c_1 \cdot r}\right) \end{aligned} \tag{2.8}$$

It is useful to predict the performance of slipper through analytical equations. However, multiple simplifications need to be done in order to do so. One of the inputs to predict the performance is the load on the slipper-swashplate interface (bearing), which requires a free body diagram of the slipper. Figure 2.7 illustrates the free body diagram of slipper. The largest force F_{KS} comes from the piston to slipper and is also named clamping force.

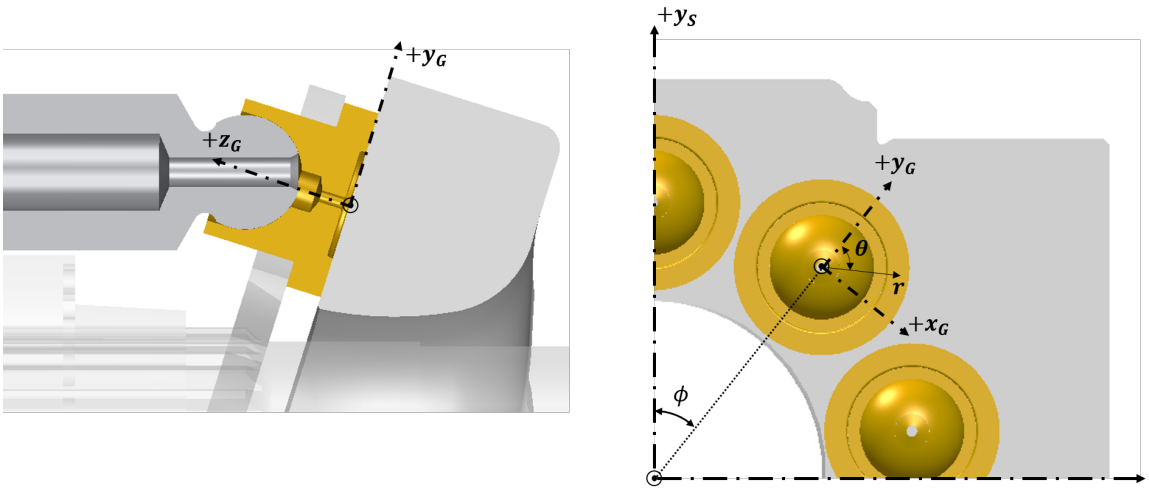

Fig. 2.6.: Slipper's local coordinate system

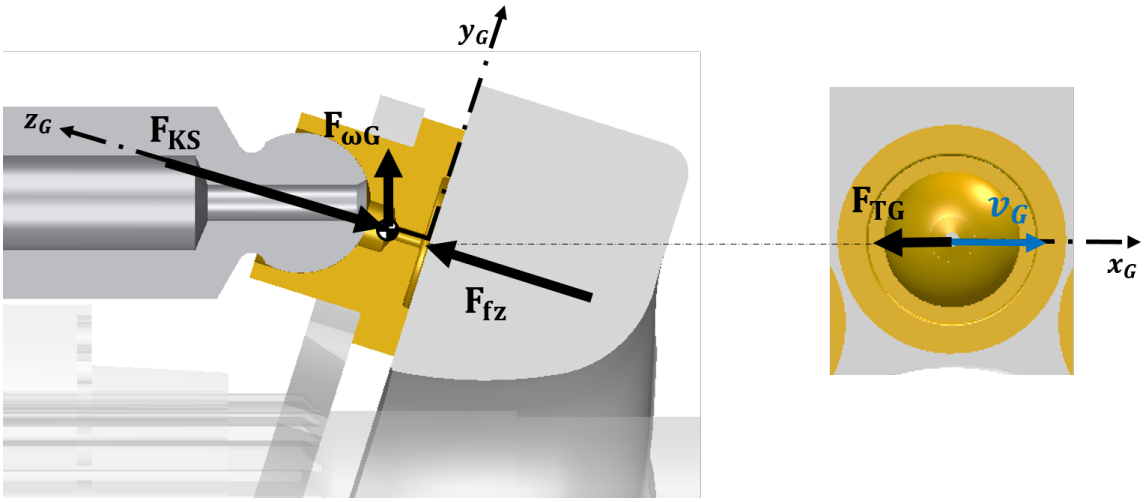

Fig. 2.7.: Slipper free body diagram

F_{KS} originates from a few sources (refer to Figure 2.8), mainly displacement chamber pressure acting on piston's end, F_{DK} which pushes the piston body in axial direction causing inertia force of piston F_{aK}. Another force F_{TK} stems from the viscous friction between the piston and cylinder bore which acts in the opposite direction of piston's motion. Sum of the three forces mentioned, which are all in axial direction, will be transmitted to the swashplate through slipper. Forces F_{SK} and F_{KS} are equal

in magnitude but opposite in direction. Due to the inclination of the swashplate, the force F_{SK} is at an angle β. It is of value to find the value of F_{KS} since it would be the main load borne by the thin film. From the piston's free body diagram, it can be seen that:

$$F_{SK_x} = F_{DK} + F_{aK} + F_{TK} = \frac{\pi}{4}({d_K}^2 - {d_{dG}}^2) \cdot p_{DC} + m_K \cdot a_K + F_{TK} \tag{2.9}$$

From the above forces, F_{TK} needs to be calculated from a numerical model unless it is the piston is concentric to the cylinder. Due to this reason, F_{TK} is neglected in the analytical approach later in this chapter. Once the x-component of F_{SK} is found, F_{SK} can be easily derived:

$$F_{SK} = \frac{F_{SK_x}}{\cos(\beta)} \tag{2.10}$$

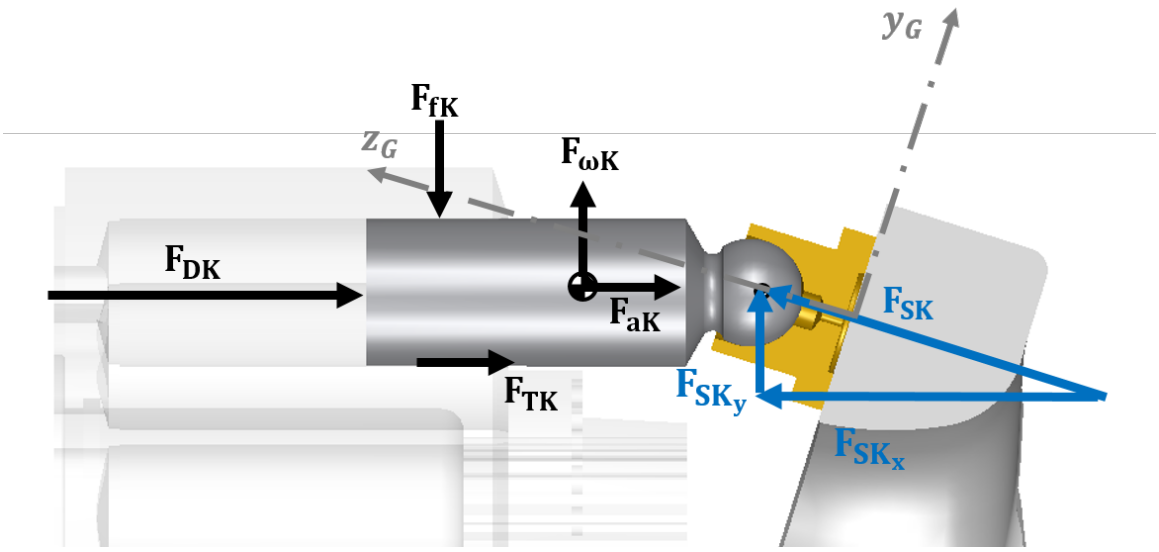

Fig. 2.8.: Piston free body diagram

Once the load is determined, an analytical model can be derived. However, other forces shown on the free body diagrams of slipper and piston will be briefly described first. On slipper's free body diagram, $F_{\omega G}$ is the centrifugal force due to rotation of

slipper around the pump shaft pointing outwards. This force tips the slipper in such a way that the thin film increases along the positive y_G axis. F_{TK} is the friction force between the slipper and swashplate that due to the complexity of thin film thickness, is calculated numerically. F_{fz} is the force due to the pressure of thin film and pocket pressure on their respective areas which is the also calculated in the numerical model. Moving over to the piston's free body diagram, F_{fK} is the force due to the pressure of thin film between the piston and cylinder. $F_{\omega K}$ is the centrifugal force of the piston due to its rotation around the shaft.

Analytical Approach

Large forces generated due to displacement chamber will push the piston to the swashplate and lack of a proper design to bear this load and transmit to the swashplate can cause large losses and inefficiencies. An analytical analysis to predict the performance of this interface is beneficial in understanding the validity of the design. To arrive at an analytical solution to such a complex system, multiple assumptions need to be made to simplify different phenomena happening in this lubricating interface. The main force that needs to be borne, ignoring $F_{\omega G}$ and F_{TG}, is as follows:

$$F_{KS} = \frac{\pi}{4 \cdot \cos(\beta)}({d_K}^2 - {d_{dG}}^2) \cdot p_{DC} + F_{HD} \tag{2.11}$$

where F_{HD} is the hold down force assuming the pump uses this mechanism since there is also a fixed clearance hold down mechanism. Assuming a slipper design with one sealing land and parallel to the swashplate, an analytical solution for the pressure distribution can be found (Hamrock, 2004) as a function of radial distance, r:

$$p = p_G \frac{\ln(r/r_{outG})}{\ln(r_{inG} - r_{outG})} \tag{2.12}$$

where r_{inG} and r_{outG} are $d_{in}/2$ and $d_{outG}/2$, respectively. Once pressure distribution in the sealing land region is calculated, it can be integrated over the sealing land area and combined with the force of slipper pocket pressure on the pocket area to find the fluid force in the thin film:

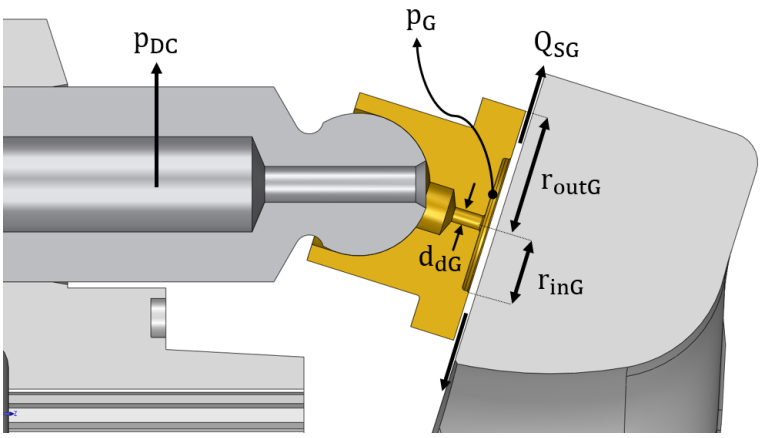

Fig. 2.9.: Slipper leakage and orifice

$$F_{fz} = \pi \cdot {r_{inG}}^2 \cdot p_G + \int_{r_{inG}}^{r_{outG}} p_G \frac{\ln(r/r_{outG})}{\ln(r_{inG} - r_{outG})} \cdot 2\pi r \cdot dr = \frac{\pi \cdot p_G({r_{outG}}^2 - {r_{inG}}^2)}{2 \cdot \ln(r_{inG} - r_{outG})} \quad (2.13)$$

This force F_{fz} is only hydrostatic and does not include any hydrodynamic effects which brings up an important factor in design of slipper-swashplate interface. Balance factor is the ratio of hydrostatic fluid forces F_{fz} over clamping force F_{KS}. If this ratio is less than 1, it means that slipper is under-balanced and if it is above 1 the slipper is considered over balanced. This value needs to be below 1 since during operation hydrodynamic pressure generation will add up to the fluid forces and can make up for the deficit to balance out the slipper and prevent contact. Two important factors in determining the performance of the slipper-swashplate interface are leakage and viscous friction. Leakage contributes to volumetric inefficiencies and viscous friction contributes to torque loss. The values of slipper leakage from the interface and viscous friction are defined as follows (Hammrock, 2004):

$$Q_{SG} = \frac{\pi \cdot {h_G}^3 \cdot p_G}{6\mu \cdot \ln(\frac{r_{outG}}{r_{inG}})} \quad (2.14)$$

$$F_{TG} = \int_A \tau \cdot dA = \mu \frac{R_B \cdot \omega}{h_G} \pi({r_{outG}}^2 - {r_{inG}}^2) \quad (2.15)$$

Consequently, the power loss due to each of these two factors, Q_{SG} and F_{TG} can be found as follows:

$$P_{Q_{SG}} = Q_{SG} \cdot p_G = \frac{\pi \cdot {h_G}^3 \cdot {p_G}^2}{6\mu \cdot \ln(\frac{r_{outG}}{r_{inG}})} \tag{2.16}$$

$$P_{F_{TG}} = F_{TG} \cdot \omega \cdot R_B = \mu \frac{\omega^2 \cdot {R_B}^2}{h_G} \pi ({r_{outG}}^2 - {r_{inG}}^2) \tag{2.17}$$

Combination of these two sources represents the total power loss. Solely based on the analytical approach, through many assumptions, one can decide if a certain slipper-swashplate interface is efficiently designed. Although the accuracy of this approach is the key point here; due to thermal and pressure deformations of slipper and swashplate bodies, film thickness of slipper can only calculated accurately through numerical models. Therefore this assumption of parallel slipper and swashplate is also invalid; hence the development of a novel fluid-solid-thermal interaction (FSTI) model by Schenk (2014) which is the base of this study. Next, the details of this model will be discussed in details since it encompasses important information regarding the methodology used in this research.

3. MODEL OVERVIEW

In this chapter the details of the numerical model developed by Andrew Schenk (2014) will be discussed. Although there were no contributions to this work by the author that were used during the study, it is important to understand the underlying physics of the lubrication phenomena in slipper-swashplate interface. An overview of the model is provided in Table 3.1. Each of the models will be briefly discussed in this chapter. To learn about the derivations of the equations and more details, refer to A. Schenk (2014).

Table 3.1.: Numerical models in the FSTI

Model	Model Details
Gap Pressure Model	-Reynolds -FVM discretization 2D
Slipper Pocket Pressure Model	-Pressure Build-up Equation
Temperature & Viscosity Model	-Energy Equation -FVM Discretization 3D
Solid Body Deformation Model	-Elasticity Eq -FEM Discretization
Solid Body Thermal Model	-Conductive Heat Transfer -FEM Discretization -Thermal Forces
Macro Motion of Slipper	-Equation of Motion

3.1 Gap Pressure Model

At the heart of gap pressure model is the Reynolds equation which is derived from Navier-Stokes equation utilizing continuity equation. Starting from Navier-Stokes equation in vector form:

$$\rho\frac{\partial \boldsymbol{v}}{\partial t} + \rho.\nabla \boldsymbol{v} = -\nabla p + \nabla.(\mu\nabla \boldsymbol{v}) + \boldsymbol{f} \tag{3.1}$$

Multiple assumptions are made according to lubrication theory that are mentioned below:

- Fluid inertial forces are small and therefore second term in left hand side is neglected.
- Fluid acceleration is small therefore first term in left hand side is neglected.
- Body forces are neglected therefore last term in right hand side is set to zero.

These three assumptions reduce the equation 3.1 to 3.2:

$$\nabla p = \nabla.(\mu\nabla \boldsymbol{v}) \tag{3.2}$$

Two other assumptions are made before reaching the final form of Reynolds equation used in this model which are:

- Pressure, viscosity, and density gradient are zero along the height of the fluid film $\frac{\partial(p,\rho,\mu)}{\partial z} = 0$.
- Fluid velocity gradient in x and y direction are small compared to z direction.

The final form of Reynolds equation in vector form is as following:

$$\nabla.\left(-\frac{\rho h^3}{12\mu}\nabla p\right) + \nabla.\left(\frac{\rho h}{2}(v_t + v_b)\right) + \rho v_b.\nabla h_b - \rho v_t.\nabla h_t + \frac{\partial}{\partial t}(\rho h) = 0 \tag{3.3}$$

Every term in equation 3.3 has the unit $\frac{kg}{m^2.s}$ which states the mass flow rate per unit area in the fluid film domain. The first term in equation 3.3 is mass flow due to pressure gradient in the film (hydrostatic diffusion) regarded as Poiseuille (pronounced

"pwah-SWEE") term, second term is flow rate due to surface velocities (hydrodynamic diffusion) and is regarded as Couette term, third and fourth term describe the flow rate due to squeeze effect of the surfaces, and the last term is the flow rate due to local expansion. Equation 3.3 does not have an analytical solution therefore it needs to be solved numerically. Due to the nature of the fluid film shape, a polar coordinate system is used for the discretization.The structured 2D grid of the fluid film for Reynolds equation is shown in Figure 3.1:

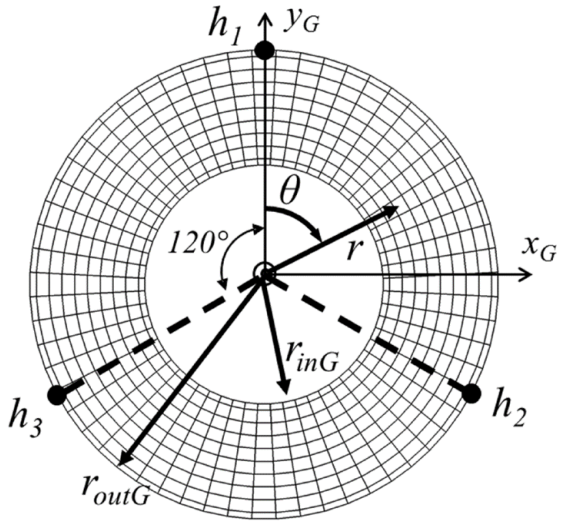

Fig. 3.1.: Structured grid for the fluid film in solving Reynolds equation (Schenk 2014)

To briefly explain the discritization, each cell (P) is surrounded by four other cells (W,N,E,S) as shown in Figure 3.2.

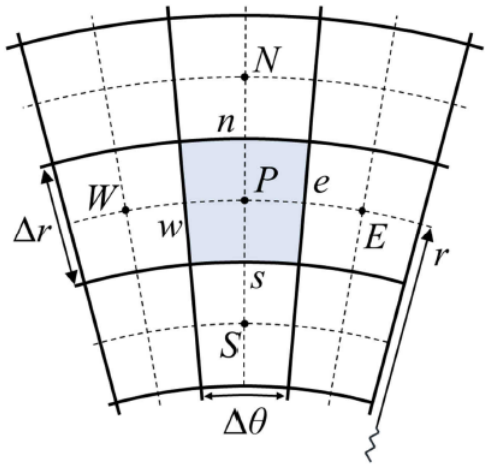

Fig. 3.2.: 2D fluid grid cells in the solution (Schenk 2014)

A modified notation of equation 3.3 in polar coordinates is presented in equation 3.4. Refer to Figure 3. for the velocity subscripts.

$$\int_\Omega \nabla.\left(\frac{h^3}{\mu}\nabla p\right) d\Omega = 12\int_\Omega \left(\begin{array}{l} \frac{h(v_{rt}+v_{rb})}{2r} + \frac{\partial h}{\partial r}\left(\frac{v_{rt}+v_{rb}}{2}\right) + h\frac{\partial}{\partial r}\left(\frac{v_{rt}+v_{rb}}{2}\right) \\ +\frac{1}{r}\frac{\partial h}{\partial \theta}\left(\frac{v_{\theta t}+v_{\theta b}}{2}\right) + \frac{h}{r}\frac{\partial}{\partial \theta}\left(\frac{v_{\theta t}+v_{\theta b}}{2}\right) - v_{rt}\frac{\partial h_t}{\partial r} \\ -\frac{v_{\theta t}}{r}\frac{\partial h_t}{\partial \theta} + v_{rb}\frac{\partial h_b}{\partial r} + \frac{v_{\theta b}}{r}\frac{\partial h_b}{\partial \theta} + \frac{\partial h_t}{\partial t} - \frac{\partial h_b}{\partial t} \end{array}\right) d\Omega \tag{3.4}$$

Using divergence theorem, left hand side of equation 3.4 is turned into the discretisized form as follows:

$$\begin{array}{l} \int_\Omega \nabla.\left(\frac{h^3}{\mu}\nabla p\right) d\Omega = \int_A \frac{h^3}{\mu}\nabla p \cdot dA = \frac{{h_e}^3}{\mu_e}\frac{\partial p_e}{r\partial\theta}\Delta r - \frac{{h_w}^3}{\mu_w}\frac{\partial p_w}{r\partial\theta}\Delta r \\ +\frac{{h_n}^3}{\mu_n}\frac{\partial p_n}{\partial r}\nabla p_n(r+\frac{\Delta r}{2})\Delta\theta - \frac{{h_s}^3}{\mu_s}\frac{\partial p_s}{\partial r}(r-\frac{\Delta r}{2})\Delta\theta \end{array} \tag{3.5}$$

Since the grid is structured and linear variable profile is assumed between cell centroids, the face pressure gradients in equation 3.5 can be found be according to the following:

$$\frac{\partial p_e}{r\partial\theta} = \frac{p_E - p_P}{r\Delta\theta}, \frac{\partial p_w}{r\partial\theta} = \frac{p_P - p_W}{r\Delta\theta}, \frac{\partial p_n}{\partial r} = \frac{p_N - p_P}{\Delta r}, \frac{\partial p_s}{\partial r} = \frac{p_P - p_S}{\Delta r} \tag{3.6}$$

By factoring centroid pressures, the pressure for cell centroid p_P as a function of four neighboring cells can be found according to equation 3.7:

$$a_P p_P - a_E p_E - a_W p_W - a_N p_N - a_S p_S = b \tag{3.7}$$

By forcing cells that are on the boundaries to have a fixed pressure value, this discretized formula can be applied to each cell to form a linear system of equations $Ap = b$ which is solved using a bi-conjugant gradient stabilized solver in GMM++ library (Renard, 2011).

3.2 Slipper Pocket Pressure Model

After finding the pressure in the sealing land, it is vital to calculate the pressure in the slipper pocket. This pressure provides the majority of the load balance for the slipper. The fluid flows from the displacement chamber through an orifice to the pocket region as shown in Figure 3.3.

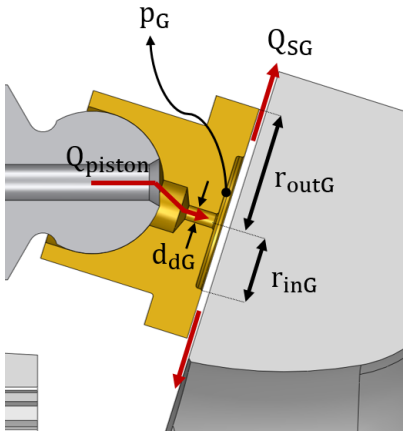

Fig. 3.3.: Flows in and out of the interface

A lumped parameter method is used to find the pressure in the slipper pocket. Eq. 3.8 which is known as the pressure build up equation relates the time derivative of pressure in a control volume with the Bulk modulus of fluid, the size of the volume, net flow, and time derivative of the volume:

$$\frac{dp}{dt} = -\frac{K}{V}\left(\sum Q + \frac{dV}{dt}\right) \tag{3.8}$$

Where K is the bulk modulus of fluid, Q is the net flow, and V is size of the control volume. Referring to Figure 3.3, the two flows are Q_{piston} and Q_{SG}. Flow in the slipper sealing land is derived according to equation 3.2 by implementing the fourth and fifth assumptions mentioned in the last section. According to the definitions of divergence and gradient operators in Eq. 3.9:

$$\begin{aligned} \nabla \cdot \boldsymbol{A} &= \tfrac{1}{r}\tfrac{\partial}{\partial r}\left(r\boldsymbol{A}_r\right) + \tfrac{1}{r}\tfrac{\partial}{\partial \theta}(\boldsymbol{A}_\theta) + \tfrac{\partial}{\partial z}(\boldsymbol{A}_z) \\ \nabla a &= \left(\tfrac{\partial a}{\partial r}, \tfrac{1}{r}\tfrac{\partial a}{\partial \theta}, \tfrac{\partial a}{\partial z}\right) \end{aligned} \tag{3.9}$$

Equation 3.2 can be broken into the following:

$$\begin{aligned} \tfrac{\partial p}{\partial r} &= \tfrac{\partial}{\partial z}(\mu \tfrac{\partial v_r}{\partial z}) \\ \tfrac{1}{r}\tfrac{\partial p}{\partial \theta} &= \tfrac{\partial}{\partial z}(\mu \tfrac{\partial v_\theta}{\partial z}) \end{aligned} \tag{3.10}$$

Using boundary conditions of $\boldsymbol{v} = \boldsymbol{v}_t$ at $z = h_t$ and $\boldsymbol{v} = \boldsymbol{v}_b$ at $z = h_b$, by integrating equation 3.10 over the fluid domain in z direction results in the velocity to be the following in vector form:

$$\boldsymbol{v} = \frac{1}{2\mu}(z^2 - (h_t + h_b)z + h_t h_b)\nabla p + z\left(\frac{\boldsymbol{v}_t \boldsymbol{v}_b}{h_t - h_b}\right) + \frac{\boldsymbol{v}_b h_t - \boldsymbol{v}_t h_b}{h_t - h_b} \tag{3.11}$$

Flow through the gap can be calculated by first analytically integrating the velocity over the film thickness in z direction and then numerically integrating over slipper circumference at the inner sealing land:

$$Q_{SG} = \int_0^{2\pi} \left(-\frac{1}{12\mu}\frac{\partial p}{\partial r}h^3 - \frac{h}{2}v_{rt}\right) r d\theta \tag{3.12}$$

The other involved in the pocket control volume is the incoming flow of Q_{piston} which according to Bernouli's equation can be defined as the following:

$$Q_{piston} = \left(\frac{2{\alpha_d}^2 \pi^4 {r_{dG}}^4 {r_{dK}}^4}{\rho(\pi^2 {r_{dG}}^4 + \pi^2 {r_{dK}}^4)} |p_{DC} - p_G| \cdot \mathrm{sgn}(p_{DC} - p_G)\right) \tag{3.13}$$

Equation 3.8 becomes the following when Q_{SG} and Q_{piston} are substituted:

$$\frac{dp_G}{dt} = \frac{K}{V_{pocket}}\left(Q_{piston} - Q_{SG} - \frac{dV_{pocket}}{dt}\right) \tag{3.14}$$

Using first order backward Euler method to solve the ordinary differential equation 3.14 results in the following formula:

$$p_G = (p_G)_{t-1} + \Delta t \frac{dp_G}{dt} \tag{3.15}$$

Only terms that are consistently being updated due to their numerical nature are Q_{SG} (gap model) and dV/dt (slipper micro motion).

3.3 Temperature and Viscosity

Viscosity plays an important role in determining the load carrying ability of a lubricating interface. Viscosity depends on pressure and temperature and its value can greatly vary by change in any of these two factors. Pressure values are already known from the gap pressure model, however temperature values are not known. To calculate the temperature distribution in the fluid film, the convection-diffusion or energy equation is used:

$$\nabla \cdot (\rho c_p v T) = \nabla \cdot (\lambda \nabla T) + \Phi_d \tag{3.16}$$

The transient effects of heat transfer are neglected since steady state is involved. The discretization of energy equation is similar to that of Reynolds equation in last section except that it is done in 3D instead of 2D. The term Φ_d is heat generation in the fluid film and is defined as the following:

$$\Phi_d = \left(\frac{\partial v_r}{\partial z}\right)^2 + \left(\frac{\partial v_\theta}{\partial z}\right)^2 + \frac{4}{3}\left(\frac{v_r}{r}\right)^2 + \left(\frac{v_\theta}{r}\right)^2 \tag{3.17}$$

Worth to mention that the heat Dissipation in Eq 3.17 is used as power loss in the FSTI code since it encompasses more factors than just power loss due to leakage and viscous friction. Once the temperature field in the fluid film is known, viscosity can be found using the Roelands (1996) equation which relates viscosity with pressure and temperature as shown in Eq 3.18:

$$\mu = 10^{\wedge}\left(G_0 \frac{(1+p/2000)^{C_2 \log(1+t/135)+D_2}}{(1+t/135)^{S_0}} - 1.2\right) \tag{3.18}$$

Where p and t are pressure and temperature, and G_0, C_2, and D_2 are empirically derived terms. There are also other models that were developed previously which could be used to increase stability of the model.

3.4 Solid Body Pressure Deformation

Once the pressure distribution in the gap has been calculated from the gap pressure model, the deformation of the slipper and swashplate surfaces due to gap pressure and thermal stress need to be determined. Although these deformations are very small, since they are on the same scale as fluid film thickness, they need to be included. In order to find the solid body deformations at each iteration due to pressure gap, the method of influence matrices (Schenk and Ivantysynova, 2011). is used to significantly save simulation time. In this method, first a fully meshed model is fed into a FEM solver (using tetrahedron elements) for elasticity equation which in weak form is expressed as:

$$\begin{aligned} &\int_\Omega \bar{u}(\nabla \cdot \sigma + b) d\Omega = 0 \\ &\sigma = D = \tfrac{E\nu}{(1+\nu)(1-2\nu)} tr(\epsilon)\boldsymbol{I} + \tfrac{E}{1+\nu}\epsilon \end{aligned} \tag{3.19}$$

Where σ is stress tensor, b is body force vector, $\bar{u}$ is weighted functions, ϵ is strain vector, E is modulus of elasticity, and ν is Poisson's ratio, An influence matrix contains an array of displacement of all the nodes when a certain amount of pressure is applied to each node separately. Using the influence matrices, each iteration the solid body deformation needs to be calculated, a combination of matrix multiplication and summation will be performed to find the total displacement of a surface. Equation 3.20 explains this method:

$$U = \sum_i \frac{p_i}{p_{ref}} IM_i \tag{3.20}$$

Where U is total surface displacement, i is the node number, and p_{ref} is the reference pressure the influence matrix is calculated based on. For the FEM discritization, tetrahedron elements are used. The element shape functions are defined as:

$$\begin{bmatrix} N_1 \\ N_2 \\ N_3 \\ N_4 \end{bmatrix} = \begin{bmatrix} 1111 \\ x_1x_2x_3x_4 \\ y_1y_2y_3y_4 \\ z_1z_2z_3z_4 \end{bmatrix}^{-1} \begin{bmatrix} 1 \\ x \\ y \\ z \end{bmatrix} \tag{3.21}$$

Solving a linear system of equations of form $Ku = b$, the element stiffness matrix is defined as:

$$K = B^T DB \tag{3.22}$$

$$B = \begin{bmatrix} \frac{\partial N_1}{\partial x} & 0 & 0 & \frac{\partial N_2}{\partial x} & 0 & 0 & \frac{\partial N_3}{\partial x} & 0 & 0 & \frac{\partial N_4}{\partial x} & 0 & 0 \\ 0 & \frac{\partial N_1}{\partial y} & 0 & 0 & \frac{\partial N_2}{\partial y} & 0 & 0 & \frac{\partial N_3}{\partial y} & 0 & 0 & \frac{\partial N_4}{\partial y} & 0 \\ 0 & 0 & \frac{\partial N_1}{\partial z} & 0 & 0 & \frac{\partial N_2}{\partial z} & 0 & 0 & \frac{\partial N_3}{\partial z} & 0 & 0 & \frac{\partial N_4}{\partial z} \\ \frac{\partial N_1}{\partial y} & \frac{\partial N_1}{\partial x} & 0 & \frac{\partial N_2}{\partial y} & \frac{\partial N_2}{\partial x} & 0 & \frac{\partial N_3}{\partial y} & \frac{\partial N_3}{\partial x} & 0 & \frac{\partial N_4}{\partial y} & \frac{\partial N_4}{\partial x} & 0 \\ 0 & \frac{\partial N_1}{\partial z} & \frac{\partial N_1}{\partial y} & 0 & \frac{\partial N_2}{\partial z} & \frac{\partial N_2}{\partial y} & 0 & \frac{\partial N_3}{\partial z} & \frac{\partial N_3}{\partial y} & 0 & \frac{\partial N_4}{\partial z} & \frac{\partial N_4}{\partial y} \\ \frac{\partial N_1}{\partial z} & 0 & \frac{\partial N_1}{\partial x} & \frac{\partial N_2}{\partial z} & 0 & \frac{\partial N_2}{\partial x} & \frac{\partial N_3}{\partial z} & 0 & \frac{\partial N_3}{\partial x} & \frac{\partial N_4}{\partial z} & 0 & \frac{\partial N_4}{\partial x} \end{bmatrix} \tag{3.23}$$

And D from equation 3.19 is expressed as:

$$D = \begin{bmatrix} 1-\nu & \nu & \nu & 0 & 0 & 0 \\ \nu & 1-\nu & \nu & 0 & 0 & 0 \\ \nu & \nu & 1-\nu & 0 & 0 & 0 \\ 0 & 0 & 0 & \frac{1-2\nu}{2} & 0 & 0 \\ 0 & 0 & 0 & 0 & \frac{1-2\nu}{2} & 0 \\ 0 & 0 & 0 & 0 & 0 & \frac{1-2\nu}{2} \end{bmatrix} \tag{3.24}$$

The final system of equation is solved using incomplete Cholesky preconditioned iterative conjugant gradient solver using the GMM++ library.

3.5 Solid Body Thermal Deformation

Once the temperature distribution in the gap has been calculated using energy equation the heat transfer, which is conduction dominantly, to the solid bodies will be determined. Once the temperature distribution in the solid bodies are known, thermal strain can be calculated which will affect the fluid film thickness. Heat transfer from the thin film which is assumed to be only in Z direction is as follows:

$$\begin{aligned} q_{swashplate} &= -\lambda\left(\frac{\partial T}{\partial z}\right)_{z=0} \\ q_{slipper} &= -\lambda\left(\frac{\partial T}{\partial z}\right)_{z=h} \end{aligned} \tag{3.25}$$

Where h is the film thickness. The weak form of conductive heat transfer similar to section 3.4 will be:

$$\int_{\Omega} \bar{T}(-\lambda \nabla T) d\Omega = 0 \tag{3.26}$$

Where $\bar{T}$ is the weighted function. The discritization of the thermal model is similar to that of section 3.4 and therefore won't be repeated. Knowing the temperature distribution of solid bodies, the elemental strain is defined as:

$$_{T} = \begin{bmatrix} \alpha_T \Delta T \\ \alpha_T \Delta T \\ \alpha_T \Delta T \\ 0 \\ 0 \\ 0 \end{bmatrix} \tag{3.27}$$

Where ΔT is temperature difference with respect to a reference temperature of 20 degrees C which is the temperature the components are sized at. The thermal force is defined as:

$$f_T = \int_V B^T D_T dV \tag{3.28}$$

Thermal forces are summed for all the nodes and are used in the elasticity equation to find the deformation.

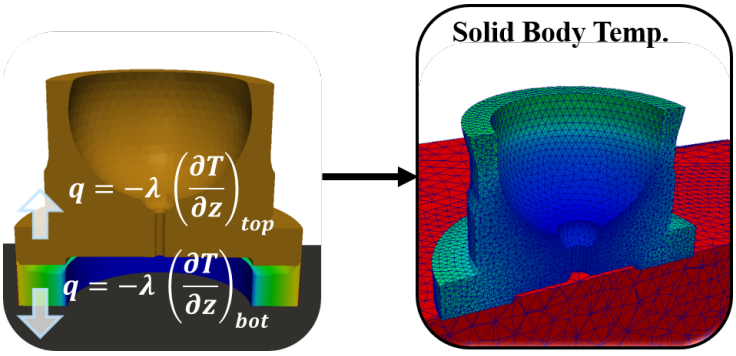

Fig. 3.4.: Heat transfer from fluid film to the solid bodies

3.6 Micro Motion of Slipper

Knowing the pressure in the gap, pocket, and the external loads on the slipper, the micro motion of the slipper can be calculated. The slipper has three degree of freedom, translation in Z direction, rotation around X and Y axes, and the equation of motion for slipper is as follows (mass and inertial tensor of slipper is small relative to forces and moments):

$$\begin{aligned} F_{fz} - F_{KS} - F_{HD} &= ma_z \simeq 0 \\ M_{fx} + M_{\omega x} &= I_x \alpha_x \simeq 0 \\ M_{fy} + M_{TG} &= I_y \alpha_y \simeq 0 \end{aligned} \tag{3.29}$$

To simplify the motion of slipper, instead three control points on the slipper outer radius are defined one located at y_G and the other two are equally distanced on the radius. The height of fluid film is defined as:

$$h_{rigid}(r,\theta) = \frac{r}{r_{outG}} \sin(\theta) \sqrt{\frac{1}{3}}(h_2 - h_3) + \frac{r\cos(\theta)}{3r_{outG}}(2h_1 - h_2 - h_3) + \frac{1}{3}(h_1 + h_2 + h_3) \tag{3.30}$$

As can be seen, this is assuming rigid body. Effects of pressure and thermal deformation on the film thickness will be added to the rigid film thickness. By taking the

time derivative of equation 3.30, the squeeze motion of the slipper (normal velocity) can be expressed as:

$$\frac{\partial h_{rigid}}{\partial t}(r,\theta) = \frac{r}{r_{outG}}\sin(\theta)\sqrt{\frac{1}{3}}(\frac{dh_2}{dt} - \frac{dh_3}{dt}) + \frac{r\cos(\theta)}{3r_{outG}}(2\frac{dh_1}{dt} - \frac{dh_2}{dt} - \frac{dh_3}{dt}) + \frac{1}{3}(\frac{dh_1}{dt} + \frac{dh_2}{dt} + \frac{dh_3}{dt}) \tag{3.31}$$

This squeez term appears in the Reynolds equation which affect the term f_{fz} in equation 3.29. To solve this system of equations, Newton's method is used to find the micro velocity that will cause a pressure force to balance the external loads. The final form of linear system of equation to be solved is as follows:

$$\begin{bmatrix} 1 & 1 & 1 \\ r_{outG} & \frac{-r_{outG}}{2} & \frac{-r_{outG}}{2} \\ 0 & \frac{-r_{outG}\sqrt{3}}{2} & \frac{r_{outG}\sqrt{3}}{2} \end{bmatrix} \begin{bmatrix} dF_{G1} \\ dF_{G2} \\ dF_{G3} \end{bmatrix} = \begin{bmatrix} F_{fz} - F_{KS} - F_{HD} \\ M_{fx} + M_{\omega x} \\ M_{fy} + M_{TG} \end{bmatrix} \tag{3.32}$$

Once the force balance is met in the slipper-swashplate interface, the shaft angle is incremented to the next angle until the whole revolution is over. As mentioned in the beginning of this section, this is a brief description of the models used in FSTI. Refer to Schenk 2014 for full description and derivation of models.

4. VIBRATION EFFECTS

4.1 Sources of Vibration

Vibration exists in axial piston pumps due to multiple sources (Kalbfleisch 2015).

- Varying displacement chamber pressure
- Shaft imbalance/misalignment
- non-uniform suction and delivery flows / fluid forces
- Varying swashplate moments due to control piston non-uniform movement
- Prime mover vibrations
- Uneven friction forces on sliding parts
- Turbulent flow force variations
- Collapsing cavitation bubbles

Out of these factors (although there could be more), varying displacement chamber pressure is the one that causes most of the vibration. According to Figure 4.1, axial forces on the piston are force from displacement chamber (F_{DK}), inertial force of piston (F_{ak}), and friction force between piston and bore (F_{TK}). Sum of these forces is named F_{AK} and is used to calculate the swashplate moments:

$$\begin{aligned} M_x &= \tfrac{R}{\cos^2(\beta)} \sum_{i=1}^{n} F_{AKi} \cdot \cos(\phi_i) \\ M_y &= R \sum_{i=1}^{n} F_{AKi} \cdot \sin(\phi_i) \\ M_z &= -R \cdot \tan(\beta) \sum_{i=1}^{n} F_{AKi} \cdot \sin(\phi_i) \end{aligned} \tag{4.1}$$

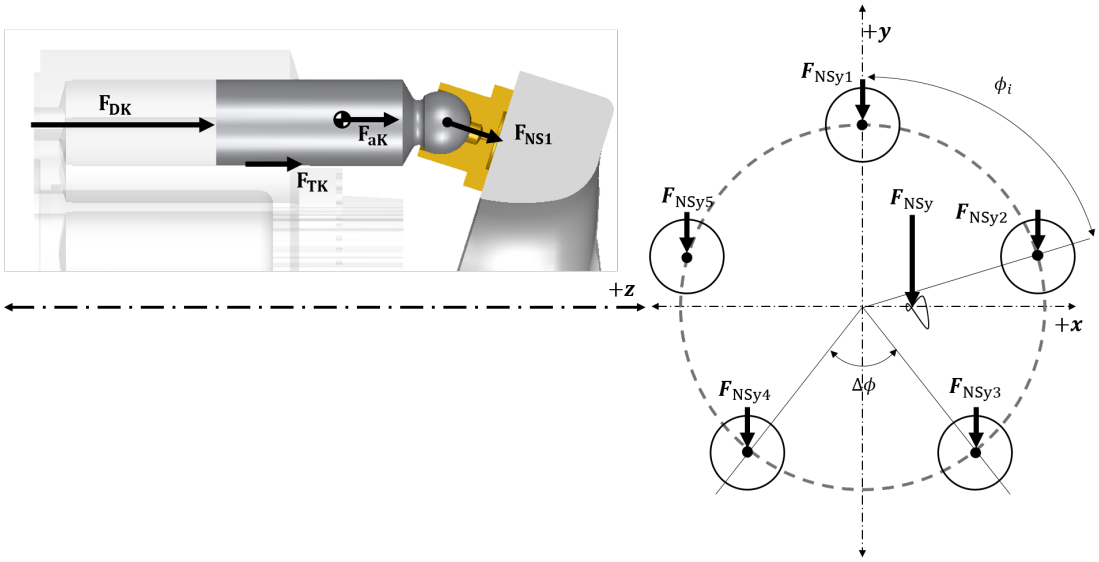

Fig. 4.1.: Forces acting on the swashplate for a pump with 5 pistons (J. Ivantysn and M. Ivantysynova 2001)

Typical values of Mx, My, and Mz are shown in Figure 4.2 for a 75 cc pump that was used for this research.

The oscillation in values of swashplate moments cause the vibration measured in this work. M_x is the largest peak to peak moment and the oscillations in the displacement chamber pressure cause the majority of the vibrations.

In this chapter, effort is made to implement the existing vibration in axial piston pumps in the slipper-swashplate interface to see its effects in the performance of the interface. Vibration can potentially change the behavior of slipper-swashplate interface in the following ways:

- a) Translating the swashplate up and down
- b) Changing the velocity of the swashplate
- c) Adding and removing force due to vibration
- d) Wearing out the ball-joint interface

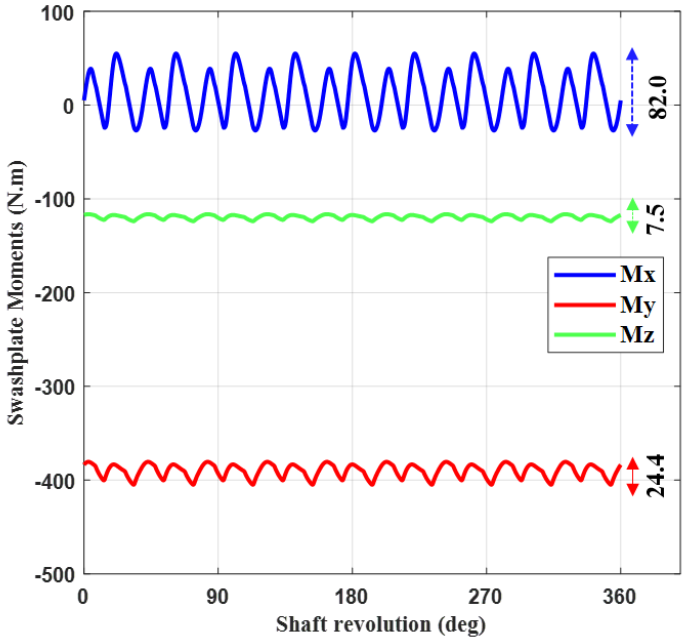

Fig. 4.2.: Moments of the swashplate for a 75 cc pump running at 1000 rpm, 100 bar dp, and full displacement

- e) Changing the external load applied to the slipper due to change of displacement chamber pressure

In this work, option "c" is chosen as the method of analysis and will be explained in detail in the next section of this chapter. In order to know how to implement the effects of vibration in slipper-swashplate interface, the value of vibration needs to be measured. The details of vibration measurement will be discussed next.

4.2 Measurement Procedure

Measurement of rotating components typically require use of a telemetry system which is expensive. Therefore the vibration of swashplate, which is stationary, was measured. The tri-axial accelerometer is mounted on the side of the swashplate as shown in Figure 4.1.

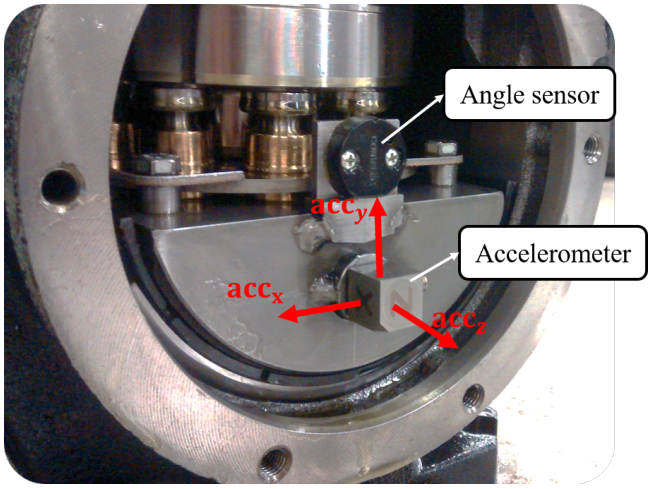

Fig. 4.3.: Accelerometer and Angle sensor location on the swashplate

Once the accelerometer was installed on the side of the swashplate, along with the angle sensor, the pump then needs to be connected to a prime mover. For this work, the prime mover is a hydraulic motor that is connected to the Maha hydraulic power supply. The Maha power supply consists of a 2000L reservoir, six electric motors, five pressure-compensated pumps and two fixed-displacement pumps. The Maha power supply is capable of delivering 300 kW of power. Taking all the safety precautions, the test rig is shown in Figure 4.3. The major components of the test rig consist of the hydraulic motor and hydraulic pump with other components such as relief valves, check valves and filters which are shown in the schematic diagram in Figure 4.4.

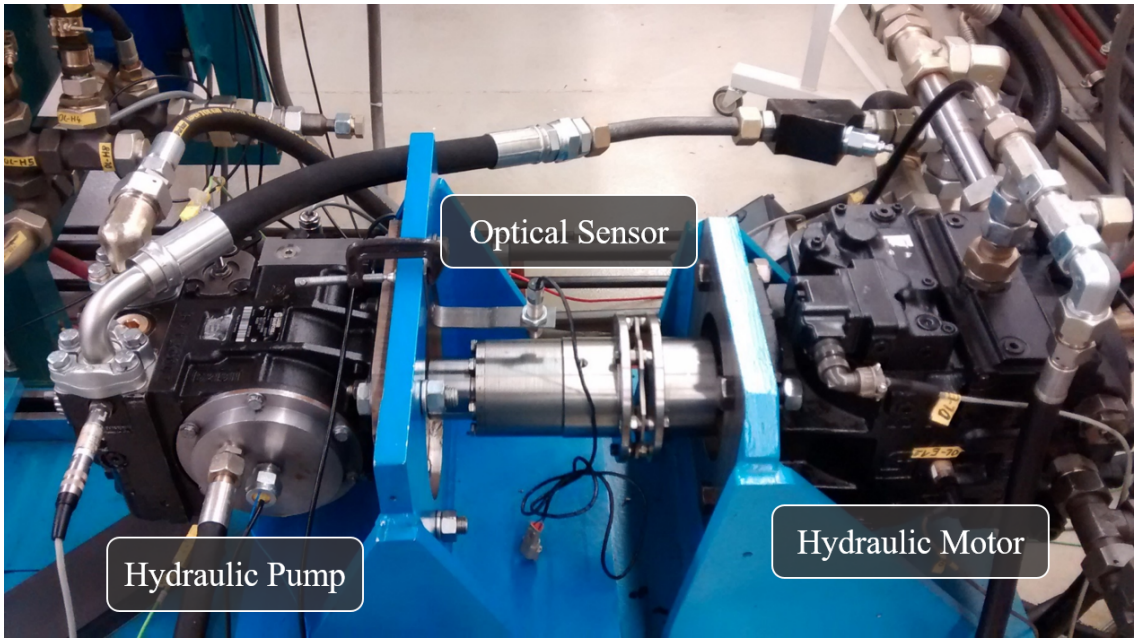

Fig. 4.4.: Test rig

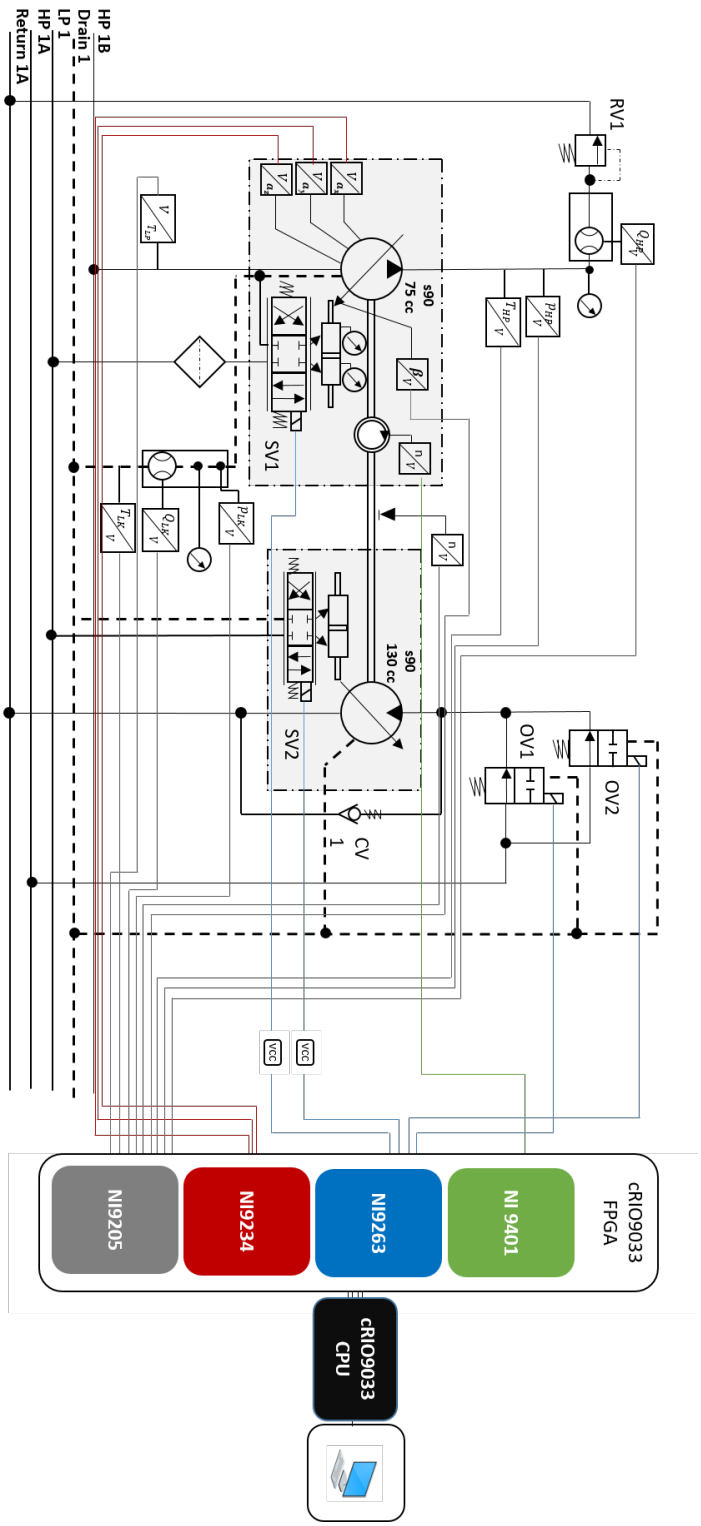

Fig. 4.5.: Schematic diagram of test rig

List of sensors used in the test rig is shown in Figure 3.5.

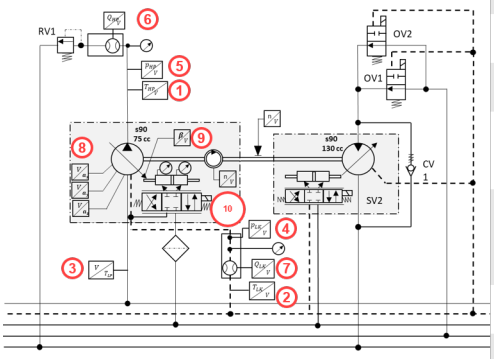

Sensor #	Model	Type	Range	Output
1,2,3	KMQSS-062G-6	K-type	-270 – 1260 ℃ (± 0.75%)	Direct
4	KELLER PA-21-50	Piezoresistive	0-50 bar	0-10 V
5	KELLER PA-21-600	Piezoresistive	0-600 bar	0-10 V
6	VS 4 GPO 12V-32N11/6	meshing gear	1 – 250 lpm (± 0.3% of value)	0-24 V
7	VS 004 GPO 12V-12A11/1	meshing gear	0.004-4 lpm (± 0.3% of value)	0-24 V
8	PCB 356A032	piezoelectric	±500 G	-5 – 5 Volts
9	Contelec Vert-X 31E	Non-contact magnet	0-360 deg	0-10 V
10	Heidenhain ROD426	quadrature encoder	0-16000 rpm	Pulse Signal
11	Monarch ROS-W	Remote Optical sensor	0-250000 rpm	Pulse Signal

Fig. 4.6.: List of sensors used in the test rig

Once all the required components were put together to form the test rig (Figure 4.5), measurements were taken for four operating conditions. Since the prime mover is also hydraulic unit and not an electric motor, with limited hydraulic oil supply, higher pressure and speed operating conditions were not possible. The operating conditions are shown in table 4.1.

Table 4.1.: Operating conditions for vibration measurement

Operating Conditions			
	dp (bar)	n (RPM)	Displacement (%)
opcon1	100	1000	100
opcon2	100	2000	100
opcon3	250	2000	100
opcon4	350	2000	100

The results of measured vibration for the above operating conditions are presented in Figure 4.7 briefly.

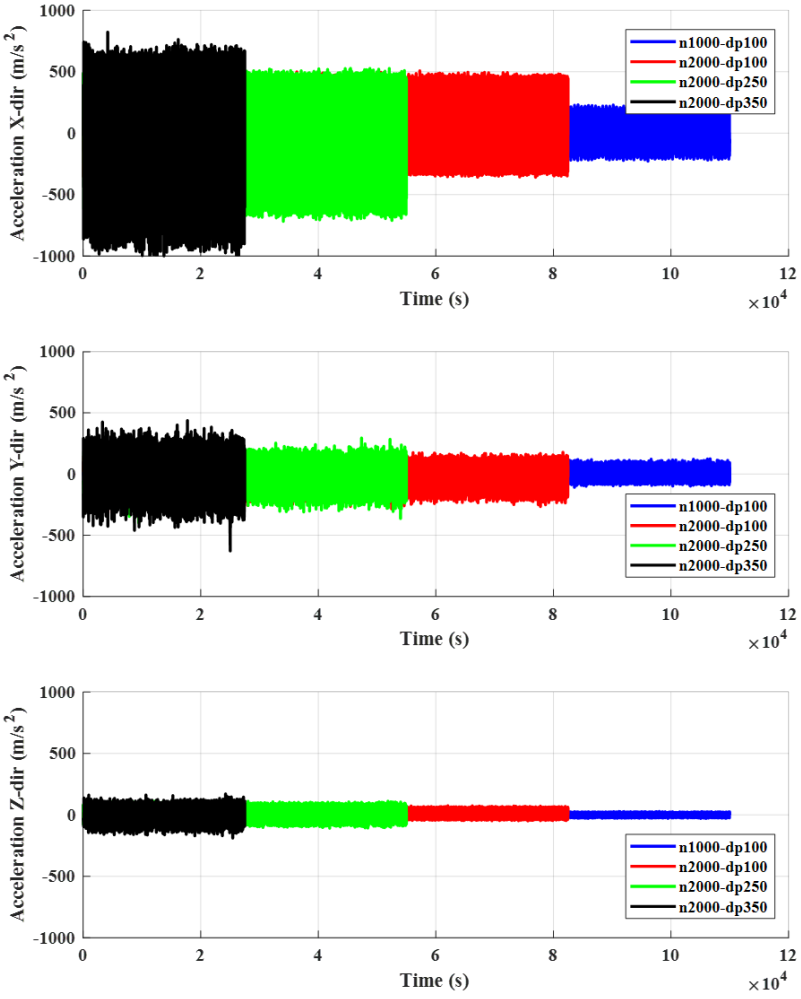

Speed(rpm)	dp(bar)	Ax(p2p)(m/s^2)
1000	100	469.5
2000	100	879.6
2000	250	1293.5
2000	350	1896.2

Speed(rpm)	dp(bar)	Ay(p2p)(m/s^2)
1000	100	247.5
2000	100	530.7
2000	250	693.5
2000	350	1137.7

Speed(rpm)	dp(bar)	Az(p2p)(m/s^2)
1000	100	60.8
2000	100	131.6
2000	250	255.4
2000	350	409.3

Fig. 4.7.: Measured swashplate vibration for operating conditions in table 4.1

4.3 Vibration Implementation as an External Load

To implement the vibration into the slipper-swashplate interface as external load, the value of vibration is multiplied by the corresponding mass to give a force. Since in FSTI swashplate is a stationary object with no movements, these effects have to be on the slippers. From the perspective of swashplate, the slippers are vibrating at the same values measured for the swashplate. For each slipper then, the external

force from vibration would be piston-slipper assembly mass multiplied by a modified version of the measured swashplate acceleration. The external force in the slipper-swashplate interface is in the Z_G direction (Figure 2.6). Therefore, all the components of vibration need to be translated to the Z_G axis. a_z is already aligned with Z_G, therefore it needs no alternation. a_y is perpendicular to the Z_G axis, therefore its contribution is zero. a_x which is the highest in magnitude, needs to be translated to Z_G axis. According to Figure 4.8, the modification to a_x is as follows:

$$a_{(Z_G)_x} = a_x \cdot \frac{R_b}{d} \cdot \cos(\phi) \tag{4.2}$$

The force added to the external load $F_K S$ (Figure 4.1) is then:

$$F_{KS}{}' = F_{KS} + m_K \cdot (a_{(Z_G)_x} + a_z) \tag{4.3}$$

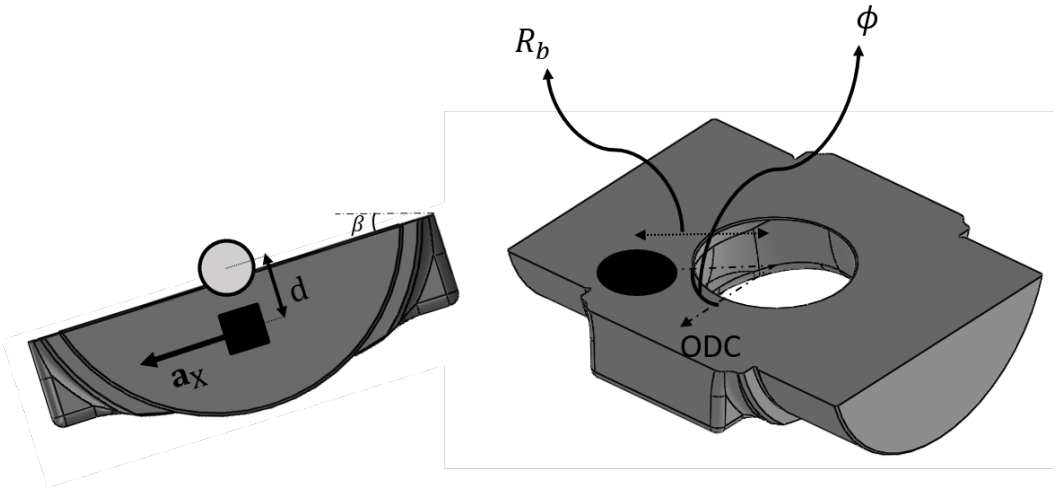

Fig. 4.8.: Translation of a_x to Z_G

It is important to know the value of vibration at any given rotation angle (ϕ). For this reason, an optical sensor was installed on the test rig to record a signal every time a particular piston makes a full rotation at ODC (outer dead center). The alignment of the piston and optical sensor is shown with red dotted line in the Figure 4.10:

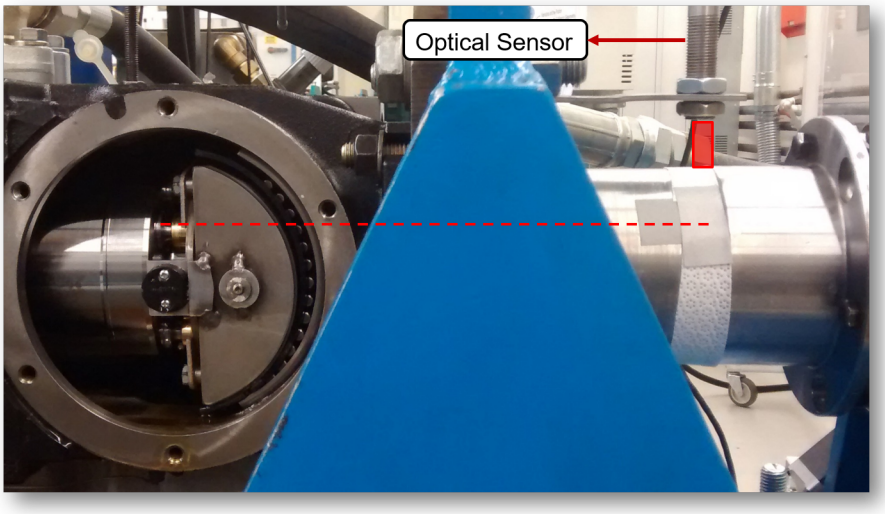

Fig. 4.9.: Piston alignment and optical sensor

An output of the optical sensor is shown in Figure 4.11. Whenever the output signal is about 0, the optical sensor is passing by the center of the reflective tape. Once the vibration signal and optical sensor signal are overlapped, the time at which piston is at ODC (ϕ=0) will be known. There is one important difference between the acquisition of optical sensor and accelerometer signal, and that is their sampling frequency. The sampling frequency of vibration is about 10240 Hz and the sampling frequency of optical sensor is 100 Hz.

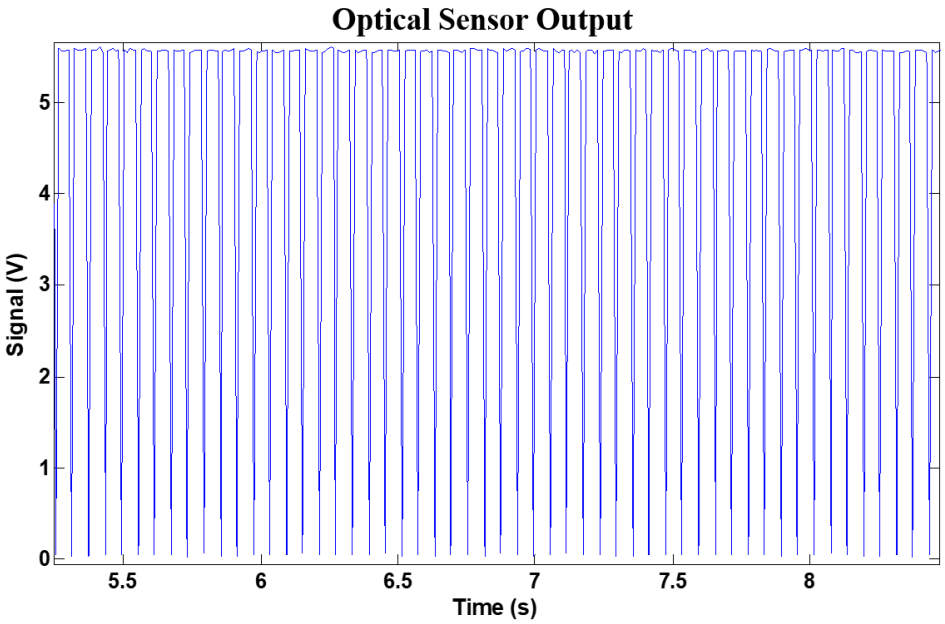

Fig. 4.10.: Output of optical sensor

Vibration signals were sorted out for many revolutions in a column-matrix. Ideally these columns should be the same, have the sampling frequencies been the same. Once plotted as transparent lines, to see the dominant signal shape, a general shape could be determined (Figure 4.12).

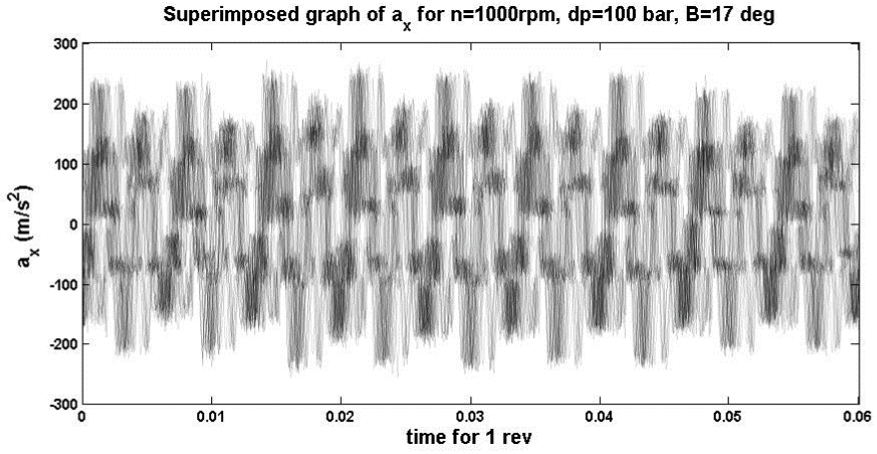

Fig. 4.11.: Superimposed vibration signal

Although this method is only graphical, it's the basis for the cross-correlation done afterwards. As it can be seen, majority of the signals start between -100 and -200

m/s^2. Finding the column that looks similar to the graphical signal in Figure 4.12 and cross-correlating the rest of the columns according to it yields the following graph in Figure 4.13 which shows that the signals were repeatable. Vibration is then used as input in FSTI as a text file.

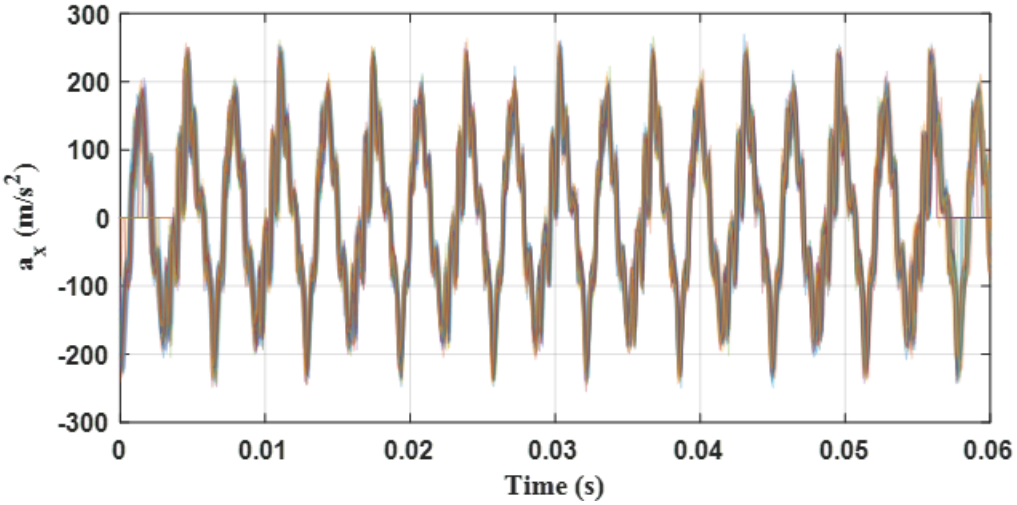

Fig. 4.12.: Superimposed vibration signals after cross-correlation was done

4.4 RESULTS

4.4.1 "n = 1000 rpm, dp = 100 bar, β = 100%"

Once vibration was implemented in the slipper-swashplate interface, the performance of the interface needs to be compared with the case with no vibration. Film thickness, viscous friction, leakage, and total power loss along with their average values are the parameters that will be compared. The operating conditions are the ones that the measurements were taken in (Table 4.1).

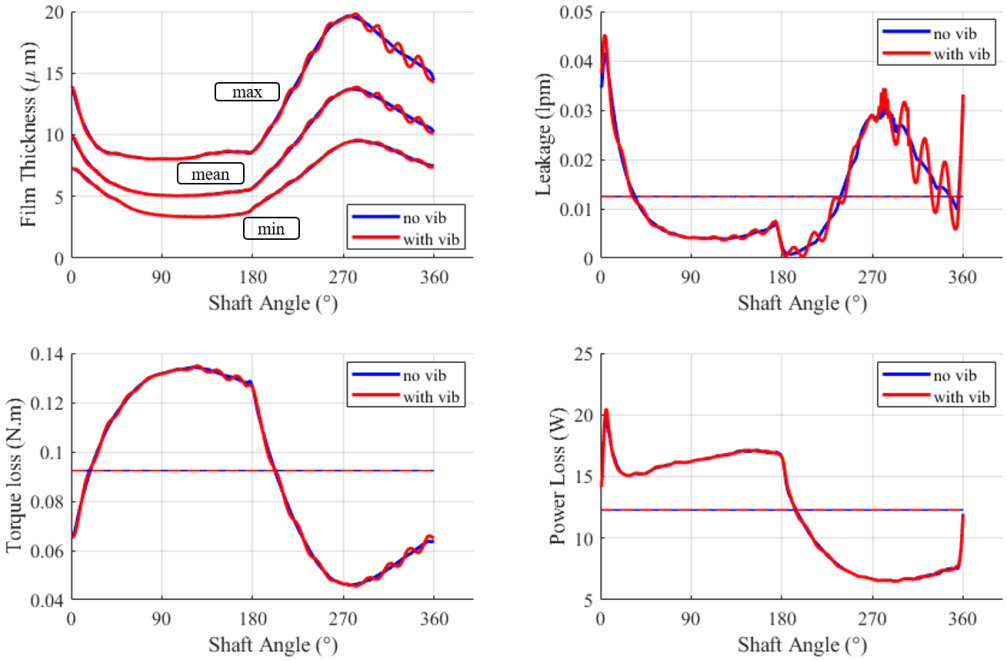

Fig. 4.13.: Performance comparison of for n = 1000 rpm, dp = 100 bar, $\beta = 100\%$

There are some small oscillations in film thickness, specially in maximum film thickness. The importance of showing film thickness is to know if the film collapses. As seen above, minimum film thickness is well above 0 micron. The most obvious difference is in the leakage, where vibration causes the leakage to oscillate heavily, although the overall leakage for the case with vibration and without vibration is the same as shown by the horizontal mean line of both curves. As for torque loss and power loss, there is no change except for very small oscillations in torque loss. From 0 to 180 degrees, the pressure in the displacement chamber is high and from 180 to 360 degrees, it's low. The reason there are more oscillations in the low pressure region, is due to the fact that external load on the slipper is less during this time, which makes the ratio of inertia force of slipper-piston assembly due to vibration higher. This applies to all the results presented ahead also.

4.4.2 "n = 2000 rpm, dp = 100 bar, β = 100%"

By doubling the speed, the performance of the interface changes as shown in Figure 4.15. Film thickness increases on average, meaning leakage also increases from the previous operating condition.

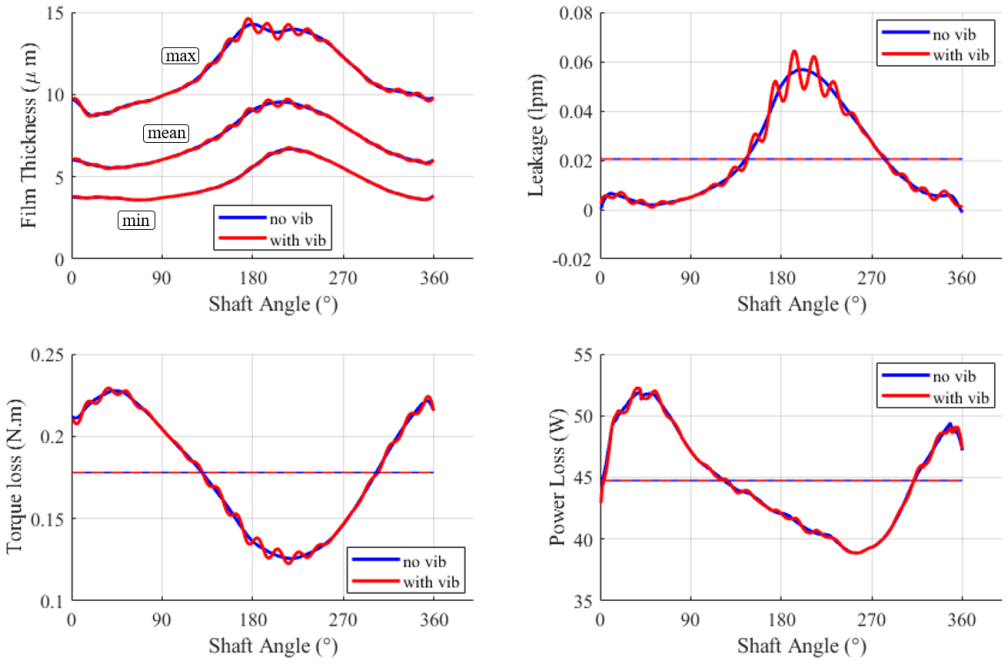

Fig. 4.14.: Performance comparison of for n = 1000 rpm, dp = 100 bar, β = 100%

Similar to previous operating condition, oscillations in the film thickness are present. Overall leakage doesn't change although there are oscillations in the low pressure region.

4.4.3 "n = 2000 rpm, dp = 250 bar, β = 100%"

Figure 4.16 shows the performance comparison for this operating condition.

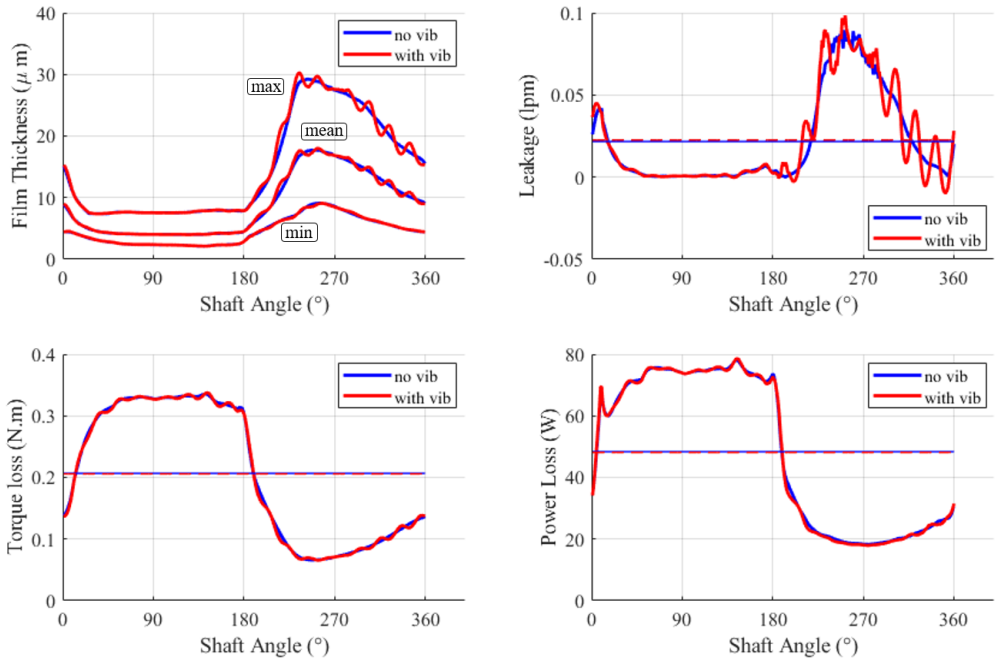

Fig. 4.15.: Performance comparison of for n = 2000 rpm, dp = 250 bar, $\beta = 100\%$

The oscillations of film thickness exist as they did for other operating conditions. However they look more explicit in the leakage results, and they cause no change in the overall value of leakage. Torque loss and power loss show very small oscillations but the mean value stays the same.

4.4.4 "n = 2000 rpm, dp = 350 bar, $\beta = 100\%$"

Figure 4.17 shows the performance comparison for this operating condition.

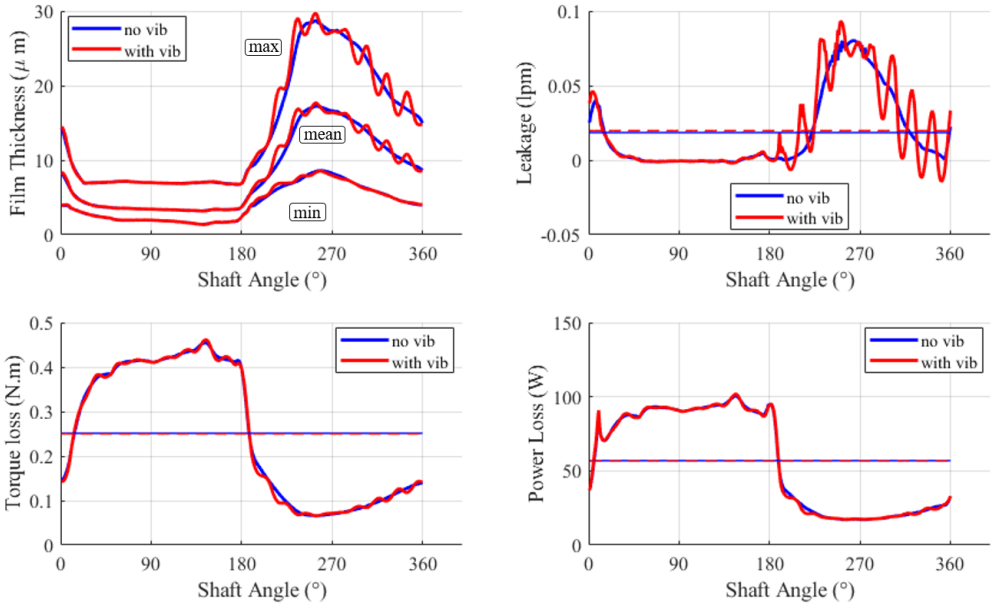

Fig. 4.16.: Performance comparison of for n = 2000 rpm, dp = 250 bar, $\beta = 100\%$

Similar pattern of results for this operating condition as compared to the previous ones. However, the magnitude of oscillations have increased for both film thickness and leakage. The average value of all the parameters stays the same.

4.4.5 Conclusion

As observed through the figures in the results section, vibration only causes oscillations during the low pressure stroke and the overall performance of the slipper-swashplate interface does not change. Due to the nature of the model being steady state, transient effects of vibration could not be captured. Moreover, there could be other methods to implement the data presented in this chapter to account for effects of vibration in the slipper-swashplate interface. One proposed method is to include the swashplate vibration in pressure build up in the displacement chamber. Using this method, the pressure in displacement chamber will change and therefore external loads in the slipper-swashplate interface will vary resulting in a change in behavior of fluid film.

5. SLIPPER SURFACE GEOMETRY

5.1 Lubricating Interface Performance Factors

There are a lot of factors that affect the performance of a lubricating interface, however there are only a few "design" parameters that can affect this performance. Aside from analyzing the working fluid and the geometric dimensions of the surfaces, the characteristics of the solid surfaces are of interest. Material, micro and macro shaping are some factors that make up the characteristics of lubricating surface. Macro shape is the overall shape of the sliding surfaces in the interface whereas the micro shape is the patterns repeated in the macro shape such as different finishes and waviness. In this work, macro shape of the slipper surface is studied and its effect on the performance of the lubricating interface will be discussed.

Slipper-swashplate interface is mostly balanced hydrostatically (85-100%). An overbalanced slipper design will result in an exceeding amount of slipper lift and leakage which increases losses. Therefore, most of the slipper designs are under-balanced with the remaining balancing share to be taken by hydrodynamic effects. If an under-balanced slipper is flat, there has to be tilt for it to operate properly and not collapse. However with pressure being higher where film thickness is lower (assuming same viscosity), there will be a moment that counters the tilt and slipper will collapse. In practice, the trailing edge will have more viscous friction and higher temperature which result in lower viscosity which could potentially make this work. However, usually flat slippers undergo decent amount of wear before they reach steady state performance which implies flat slippers don't remain flat in operation.

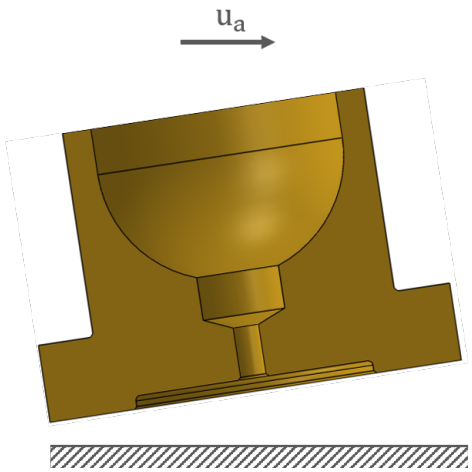

Fig. 5.1.: Flat slipper tilt

The high-pressure fluid film in the slipper/swashplate interface separates the solid bodies. The fluid pressure is created by two sources. Hydrostatic pressure which is the main source of pressure in the fluid, is provided to the slipper pocket from the displacement chamber through a series of channels in the piston/slipper assembly. Separately, hydrodynamic pressure develops in the interface because of the unparalleled surface boundary and the relative macro and micro motion between slipper and the swashplate. Slipper surface geometry in slipper-swashplate interface affects the film thickness gradient which corresponds to hydrodynamic pressure build-up. Once the load is balanced, effort needs to be minimize the losses in the interface. A slipper-swashplate interface design can be designed in such a way that it works in definitively but with very high leakage losses or viscous friction losses. Finding a design that can find the perfect balance between viscous friction and leakage is the aim of this chapter.

An optimal slipper design should minimize energy dissipation while maintaining a stable fluid film to prevent contact and/or wear of machine components. Traditional design methods involve analytical and experimental investigation of prototype slippers. Modern design approaches incorporate computational modelling into the development process. Yet, modern designs fail to prevent wear-in and contact. As a basis for this work, wear pattern of slippers from a S90 75 cc/rev commercial pump

were studied. The pump was received with slippers which had non-flat profiles. Using Mitutoyo Surftest SJ-500 profilometer according to the pattern shown in Figure 4.2, profile of each slipper was measured.

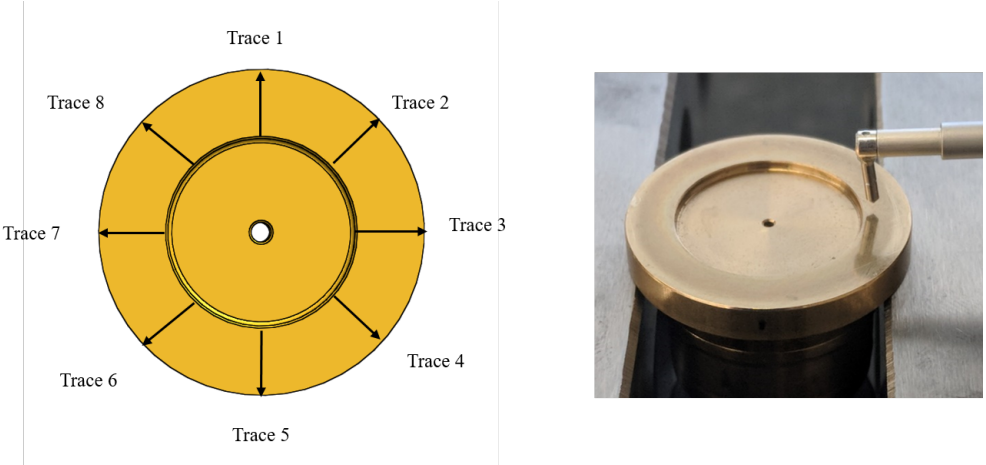

Fig. 5.2.: Measurement pattern for each slipper

Eight traces are measured for each slipper. The traces are longer than the sealing land length and are approximately 45 degrees apart. The output of the profilometer needs to be post-processed for multiple reasons. One reason is to shorten the length of data to exactly present the length of sealing land. Second reason is due to inaccuracies in the profilometer and it not being calibrated, the results are tilted therefore they need to be rotated. Figure 4.3 compares raw output from the profilometer and post-processed profile. The MATLAB code for this post-processing is shown in Appendix.

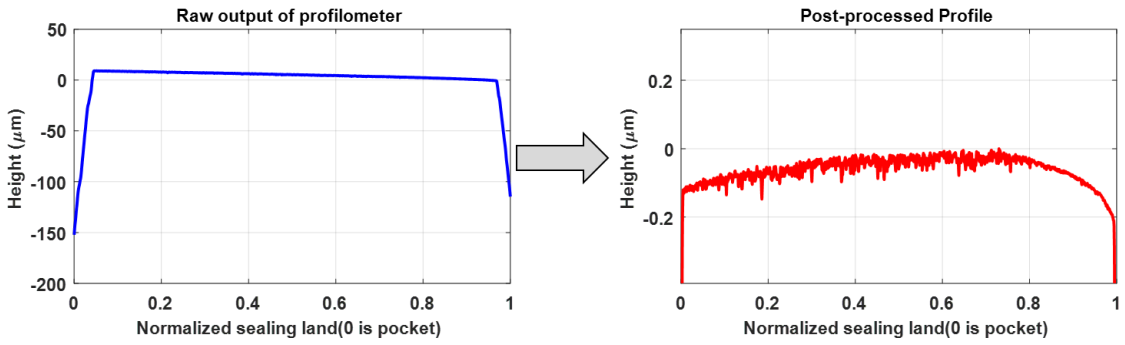

Fig. 5.3.: Raw profilometer output requires post-processing

To check the accuracy of this post-processing, a visual method was used to confirm the location of maximum height of the profile. Figure 4.4 shows black and white close-ups of slipper profiles that have gone through the wear-in process.

Fig. 5.4.: Similar wear pattern on the slipper surfaces

These pictures show a consistent pattern of wear on the slippers' surface. The dark ring is the region that has gone through the least amount of wear. That is expected as the inner and outer edges of sealing land will go through more contact. Inner sealing land is directly pushed down by the piston-ball and the outer edge makes contact once the slipper is tilted. On average, the peak is visually located at around 0.67 of normalized sealing land which matches well with the post-processed results. Now that the measurement process is explained, Figure 4.5 compares the profiles of before and after wear-in process for a certain slipper (slipper 7 in this case).

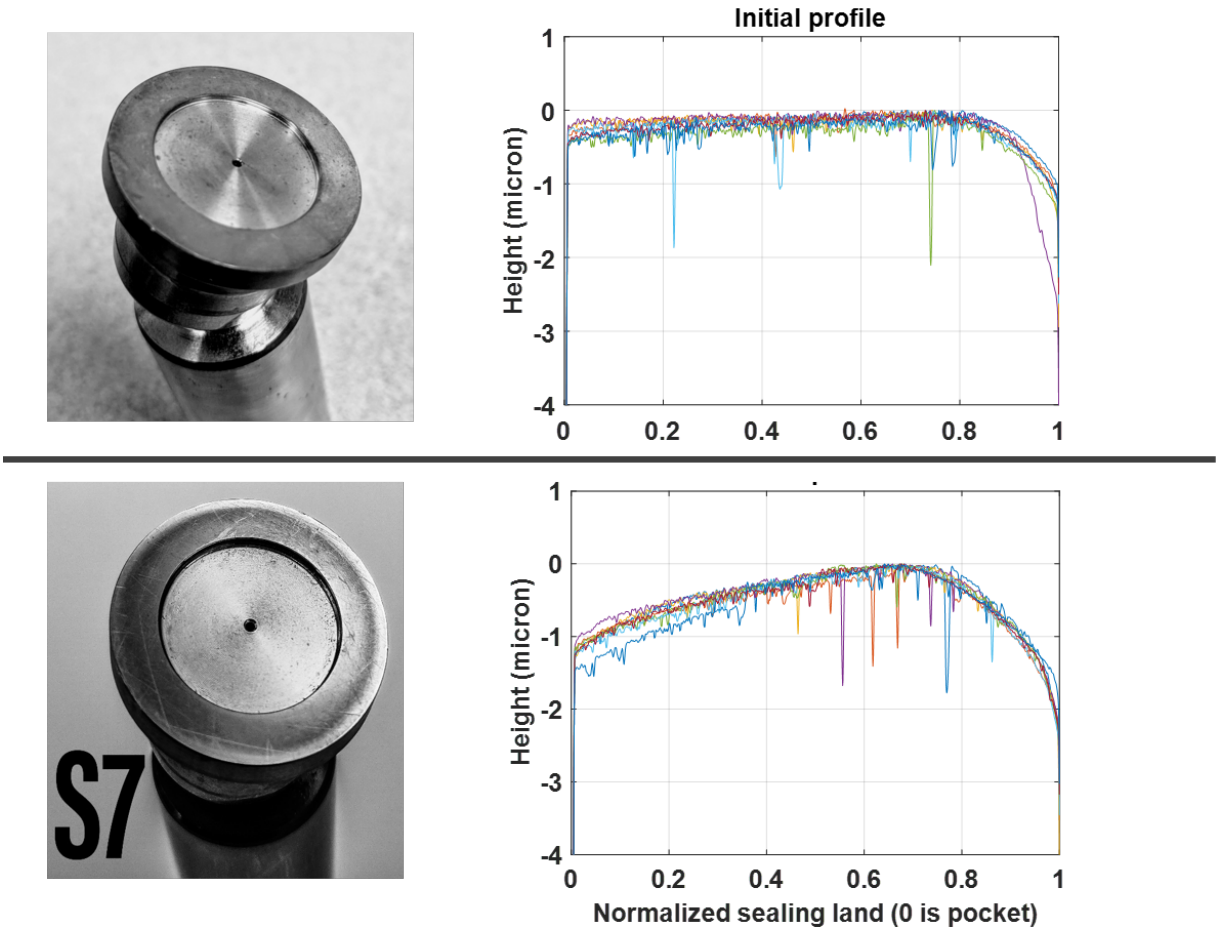

Fig. 5.5.: Slipper profile before operation (top) and after extensive operation (bottom)

The traces are consistent for both cases making the profile very clear. The spikes in the results are from tiny scratches on the surface of the slipper. Around the edge of the slipper, sometimes there are more deformations which lead to a shorter sealing land (the purple trace in the initial profile). As mentioned before, the initial profile wasn't flat. The manufacturer might have done a slight wear-in process or they might have applied a macro geometry on the slipper surfaces for the hope that they won't wear anymore. As can be seen from the results in Figure 4.5, a decent amount of wear was observed after the profile went through an operating condition of 1500 rpm, 200 bar, and 100% displacement which is a mild condition for this pump. Once this profile was measured, pump went through multiple other operating conditions that are listed in Table 4.1.

Table 5.1.: Operating conditions pump was run at after the worn-out profile

100% displacement	
dp (bar)	n (RPM)
5	500
50	1000
100	2000
200	2600
300	3200
400	-

To recap the profile history, the slipper profiles were measured when pump was received (initial profile). Then pump was run at 1500 rpm, 200 bar, and maximum displacement for about eight hours and was disassembled and the profiles were measured again (run-in profile). Pump was then put back together and ran at the all the combinations of pressure and speed presented in Table 4.1 and the profiles were measured again (post-run-in profile). There is a clear difference between the initial and run-in profile, but there is approximately no change between run-in and post-run-in profile as shown in Figure 4.6. Note that the bump in post-run-in profile at 0 sealing land is caused by measurement errors.

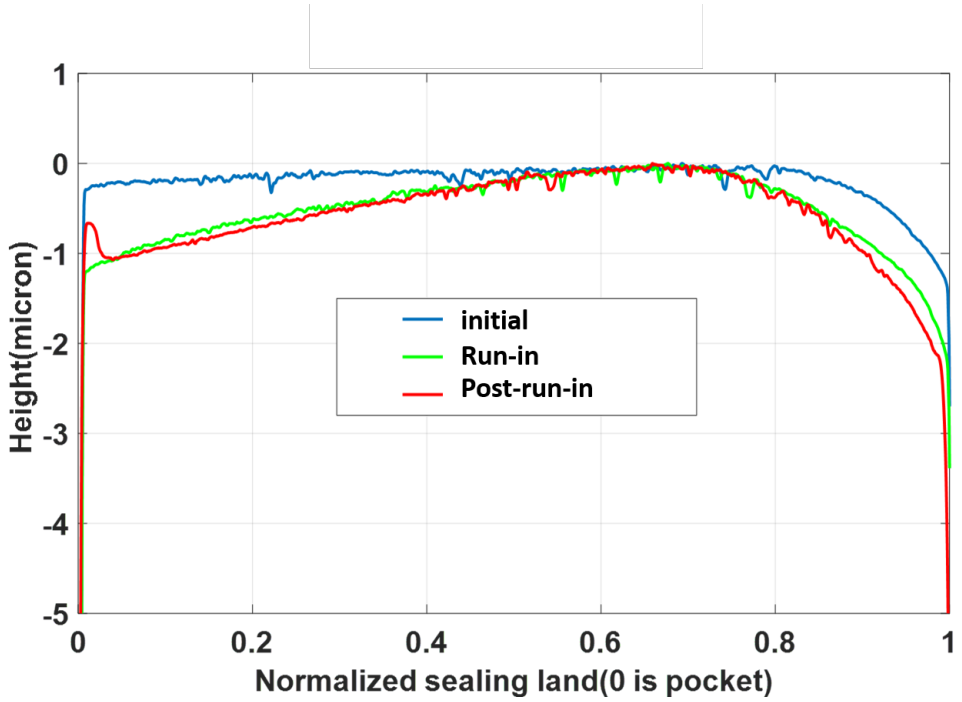

Fig. 5.6.: Comparison between three measurements of slipper profiles

These measurements were conducted to understand the change in slipper surface geometry and its patterns. These measurements were a starting point of optimizing the performance of slipper-swashplate interface by varying the surface geometry of slipper. Rest of the chapter suggests a method to prevent alterations in surface geometry due to contact of slipper and swashplate by coupling the existing numerical model (FSTI) with an optimization of slipper surface profile. The focus of this work is not on the physics and modeling of wear but on effects of slipper surface profile on the performance of the interface. When there is contact, it is likely that there is wear. However, the wearing process during operation is difficult to control, which results in a final surface profile that does not follow the intended design. In designs that don't include a macro geometry and rely on wearing process for operation, the wearing process requires a softer material usually brass which adds to the part cost. Moreover, in male slipper designs, steel is used to strengthen the ball joint neck. To avoid steel to steel contact in male slipper designs, wearing process then requires the slipper to be made bi-material (steel for the structure, brass for the running

surface), which is difficult to design, may results in unfavourable thermal behaviour, and expensive manufacturing. The aim of this paper is to provide means to design a slipper profile that prevents solid to solid contact during steady state operation while minimizing energy dissipation through use of an optimization tool coupled with FSTI model.

5.2 Optimization

Before explaining the details of the optimization, more information regarding the hydraulic pump and the simulation need to be discussed. Details of the commercial pump used for the simulation are as follows:

Table 5.2.: Details of the commercial pump studied

Parameter		Value	Unit
Displacement		75	cc/rev
Flow at rated speed		270	l/min
Torque at maximum		1.19	N.m/bar
Speed			
	Minimum	500	rpm
	Rated Speed	3900	rpm
	Maximum	4250	rpm
System Pressure			
	Max working pressure	450	bar
	Max pressure	480	bar
	Min low loop pressure	10	bar

Simulation options are provided in the Appendix. Simulations are run for 5 revolutions each which was determined to be enough number of revolutions for enough convergence.

Using the patterns of wear obtained from measurements on the slipper surface, a mathematical expression can be found to be used in an optimization scheme. The less the number of variables defining a mathematical equation for the slipper surface, less number of simulations need to be run in the future. Due to the nature of the slipper-swashplate interface, the slipper surface geometry is chosen to be axis-symmetric. The mathematical expression should be simple (as few variables as possible) and

inclusive to account for as many possible designs. To parameterize the slipper surface geometry, two quadratic splines are used. Figure 4.7 shows the curves with their variables and the equations are as below:

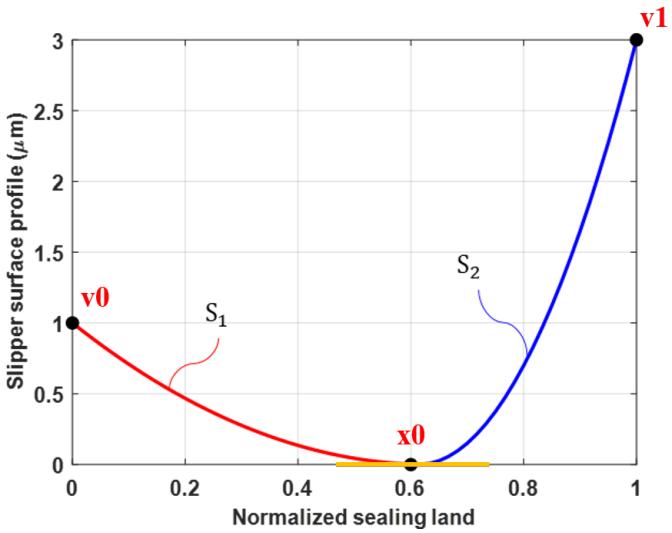

Fig. 5.7.: Comparison between three measurements of slipper profiles

$$\begin{aligned} S_1 &= a_1x^2 + b_1x + c_1 \\ S_2 &= a_2x^2 + b_2x + c_2 \\ S &= S_1 + S_2 \end{aligned} \tag{5.1}$$

As shown in Figure 4.7, three variables are used to define the curve; v0 which is value of curve at sealing land (SL) = 0, v1 which is the value of the curve at SL = 1, and x0 which is the location of minimum value of curve which also has zero slope. This curve and previous depictions of slipper surface profile (Figure 4.6) are similar just flipped upside down since the slipper is assumed to be on the swashplate in the code. With

these three variables and constraint of zero slope at x0, six unknowns of equation 4.1 can be found as follows:

$$\begin{aligned} c_1 &= v0 \\ b_1 &= -2 * \tfrac{c_1}{x0} \\ a_1 &= \tfrac{c_1}{x0^2} \\ a_2 &= \tfrac{v1}{x0^2+1-2*x0} \\ b_2 &= -2 * a_2 * x0 \\ c_2 &= v1 - a_2 + 2 * a_2 * x0 \end{aligned} \tag{5.2}$$

The objective of this optimization is to find a slipper running surface shape that eliminates contact between slipper and swashplate during steady-state operation of the axial piston machine for multiple operating conditions while minimizing power loss due to leakage and viscous friction. With only three variables; v0,v1, and x0, one constraint of no contact between slipper and swashplate, and objective of minimizing power loss, a modified full-factorial scheme is used. Other schemes such as NSGA-II and AMGA2 were also considered however since the simulations are numerically expensive ($\tilde{1}$0 hours for 5 revolutions on a Core i7-4770 @ 3.4 GHz), they were not efficient. The range of variables v0, v1, and x0 are shown in Figure 4.8:

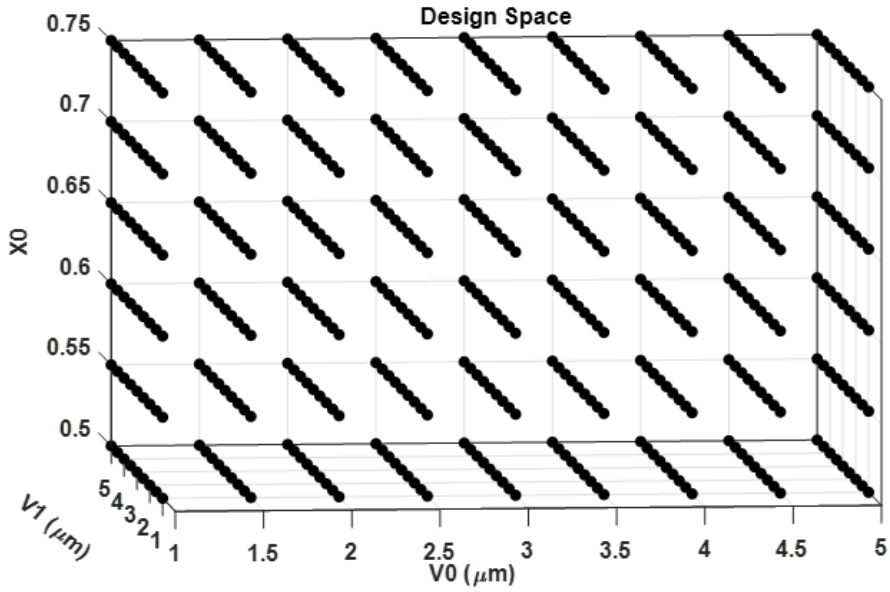

Fig. 5.8.: Range of variables v0,v1, and x0

V0 and V1 start from 1 micron because all of the designs with V0 or V1 lower than 1 micron did not pass the constraint of the optimization. Furthermore, V0 and V1 are bounded by 5 microns to eliminate the unnecessary function evaluations unfavourably high energy loss due to leakage. It should be noted that an increase in film thickness can reduce power loss at lower film thickness values due to viscous friction forces being dominant. Similarly, for the limits of X0, values below 0.5 fail to pass the optimizations constraint and X0 values above 0.75 create a sharp edge in the slipper profile for certain designs which should be avoided. The modification of full-factorial scheme will be explained after the operating conditions for the optimization are discussed. Six operating conditions (opcon) are used for this optimization which are shown in Table 4.2. This list of operating conditions cover the corner conditions with extremely low speed and high pressure.

Table 5.3.: Operating conditions used in the optimization

	dp(bar)	n(RPM)	Displacement(%)
Opcon1	450	600	100
Opcon2	450	3600	100
Opcon3	100	3600	100
Opcon4	450	600	20
Opcon5	450	3600	20
Opcon6	100	3600	20

The modification of full-factorial is as follows; All the possible combinations of variables will be run for opcon1, however only those that show no contact will pass to the next operating condition. This reduced the size of simulations to only a fraction of a full-factorial study for all operating conditions as will be shown later on in this chapter. Out of all the operating conditions, opcon1 is the most prone to showing contact since it has the highest operating pressure and displacement (load) with lowest speed (hydrodynamic effect). The flow chart of this optimization scheme is shown in Figure 4.9:

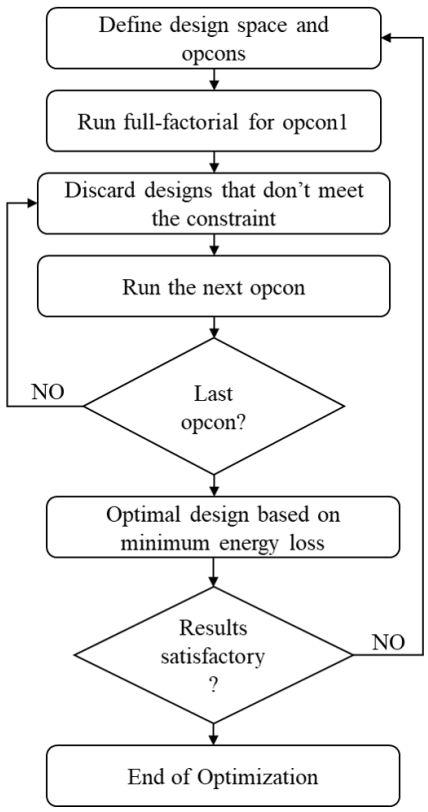

Fig. 5.9.: Optimization flow chart

The output of this optimization are slipper surface geometries that have passed the constraint check and have the lowest power loss. The optimal profile for each operating condition presented in Table 4.2 will be discussed. Moreover, one optimal profile for a slipper that goes through all the operating conditions will also be presented. The reason both of these results are important is because a pump could run through multiple operating conditions regularly or a pump can mainly operate at one operating condition. Either way, this study shows that by digitizing the performance of the pump and knowing its operating conditions, the optimal profile for its lubricating interfaces can be achieved which will eliminate solid to solid contact and give the highest efficiency to the pump. For opcon1, the screening of contact between slipper and swashplate is done by analyzing the film thickness. If the value of minimum film thickness during the whole revolution drops below 0.4 micron which is the assumed surface roughness of slipper and swashplate (0.2 micron each), then contact has oc-

curred for that slipper surface geometry. Figure 4.10 shows all the minimum film thickness plots of all 486 designs for opcon1. The red line is the optimal design's minimum film thickness. There are other film thickness traces that are lower than the optimal one during the high pressure stroke (0-180 deg), but they either increase in value during the low pressure stroke (180-360 deg) or the collapse around 340 deg.

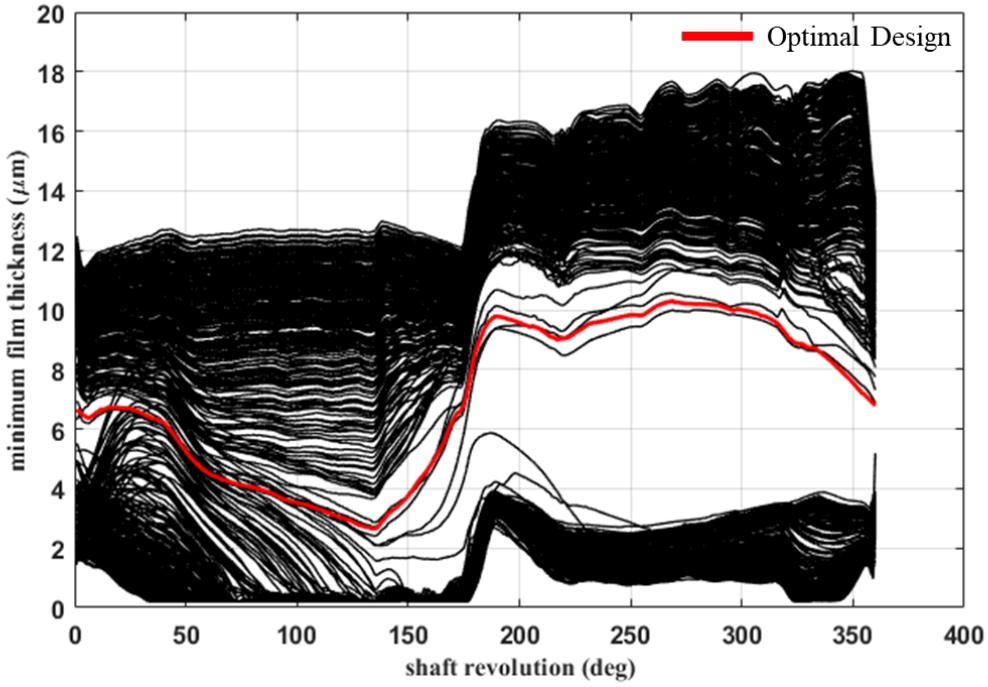

Fig. 5.10.: Minimum film thickness for all designs of opcon1

For opcon1, after the film thickness screening process, power loss will be monitored to find the design with the lowest power loss and to also analyze the effects of the three design variables on power loss. Figure 4.11 shows the power loss scatter plot vs. design number for all the operating conditions. Filled dots are the designs that show no contact and will proceed to go to the next operating condition and empty dots are designs that showed contact and their film thickness collapsed at least once during the whole revolution.

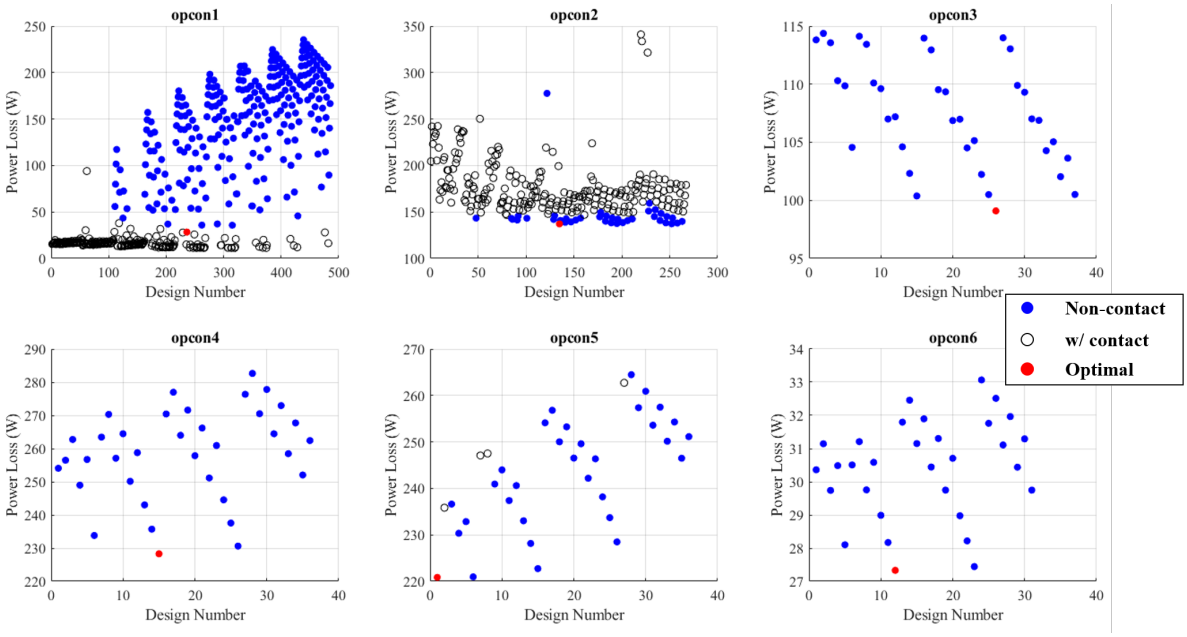

Fig. 5.11.: Design vs. power loss for all operating conditions

The optimal profile for each operating condition is presented in Figure 4.12. As the difference between the first three operating conditions and last three are only their displacement, some similarities in the pattern can be seen for the operating conditions with same speed and pressure, namely opcon2 and opcon5, along with opcon3 and opcon6. Since this wasn't a full-factorial study for each opcon and the focus of this study was to find one optimal profile that goes through all of the aforementioned operating conditions, the optimal profiles shown in Figure 4.12 are not absolute based on the variable boundaries mentioned in Figure 4.8. To further explain, the variable boundaries are changed after opcon1 and they keep getting narrower as the study goes on.

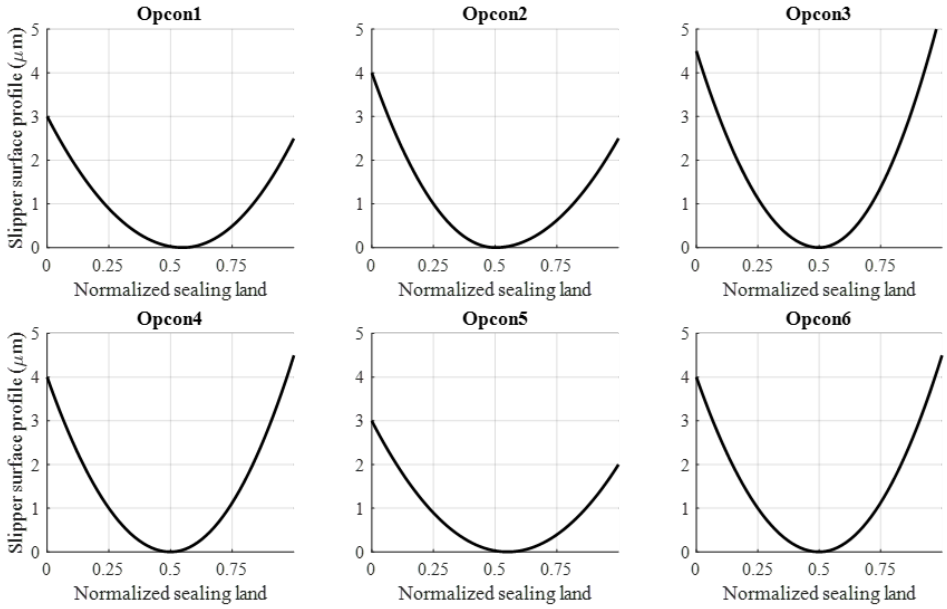

Fig. 5.12.: Optimal profiles for all operating conditions

The overall optimal profile that goes through all the operating conditions is shown in Figure 4.13 with a picture of slipper next to it for better comprehension of implementation of these profiles (Slipper is not drawn to scale).

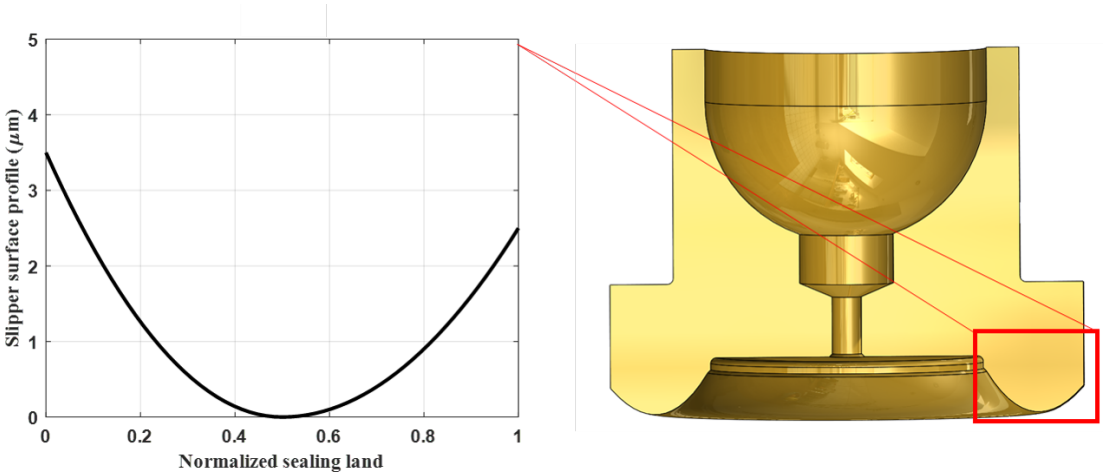

Fig. 5.13.: Optimal profile that goes through all the operating conditions

Next up will be the comparison of the performance of this optimal profile with the commercial profile initially measured in the beginning of this chapter (Fig 5.5-initial

profile). To elaborate on this comparison, each profile runs through all six operating conditions presented in this chapter (Table 5.3), then minimum film thickness, leakage, torque loss, and power loss will be compared for these profiles. As was discussed earlier, the commercial profile went through wear during operation at different operating conditions. The optimal profile is at first compared to the initial commercial profile that hasn't gone through any wear due to operation. This profile can be expressed as v0 = 0.3, v1 = 1.1, x0 = 0.8 according to the method defined earlier in this section. After this comparison, the worn out commercial profile (v0 = 1, v1 = 2, x0 = 0.7) will also be compared to the optimal profile.

It needs to be mentioned that the wear process on the commercial profile is unpredictable and does not allow for the best performance of the interface, therefore a profile that prevents contact wear should be used as the initial profile for the interface.

5.3 Results and Discussion

Starting with opcon1, the performance of commercial profile discussed earlier is compared with optimal profile shown in Figure 5.13. The results are shown in Figure 5.14.

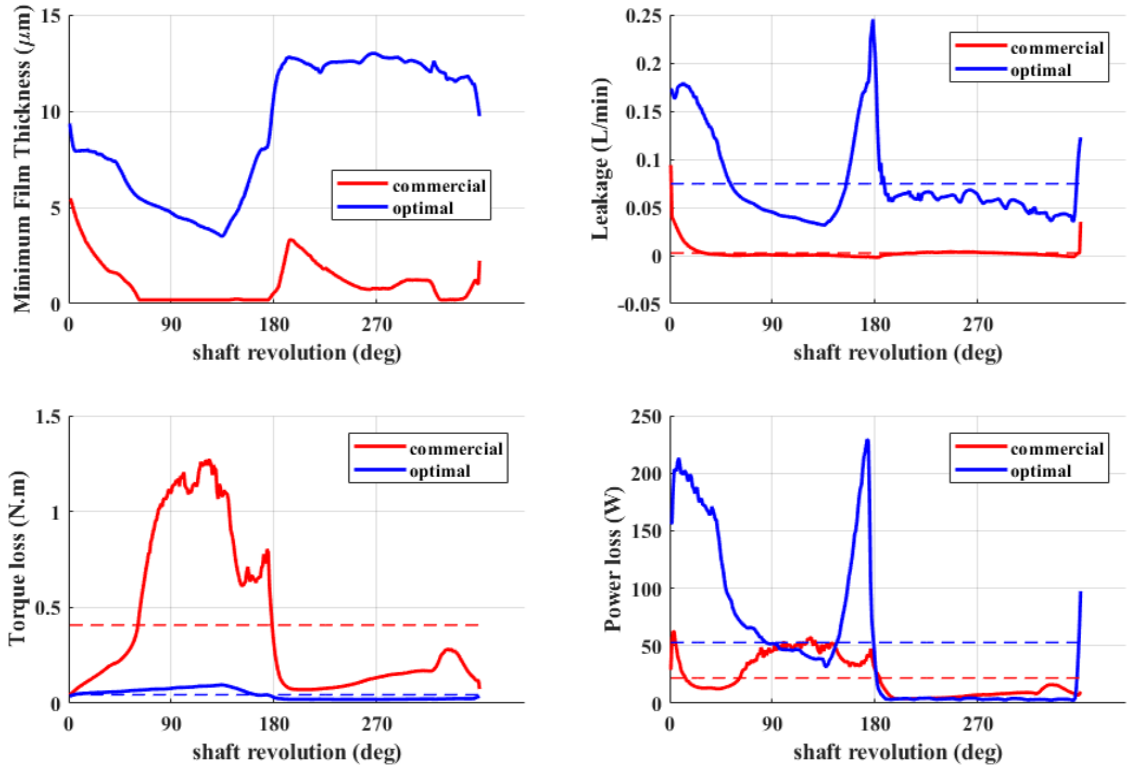

Fig. 5.14.: Comparison of performance between optimal vs commercial profile for opcon1

As discussed before, opcon1 was considered an extreme operating condition for its low speed and high pressure, which results in the commercial profile to collapse for most of high pressure stroke in the "Minimum Film Thickness" subplot. Due to this collapse, the leakage is minimal for the commercial profile whereas for the optimal profile, leakage is excessive. Moving to Torque loss subplot, the lower the film thickness, the higher is the velocity gradient term in viscous torque loss du/dh, which results in high peaks of torque loss for the commercial profile during the collapse period. Finally, the power loss plot for this operating condition (opcon1) is not in favor of the optimal profile at first look, however it needs to be stated that the commercial slipper will not operate successfully in this operating condition without going through mixed lubrication and wearing out which in its own causes power to be lost. For this result and the future ones whenever film thickness collapses, the power loss results are not

accurate and they are showing a number that is lower than what it actually should be. This discrepancy is due to the boundary lubrication and solid to solid contact which requires a different way of power loss calculation.

Moving to opcon2, Figure 5.15 at a glance shows the optimal profile as the better performer.

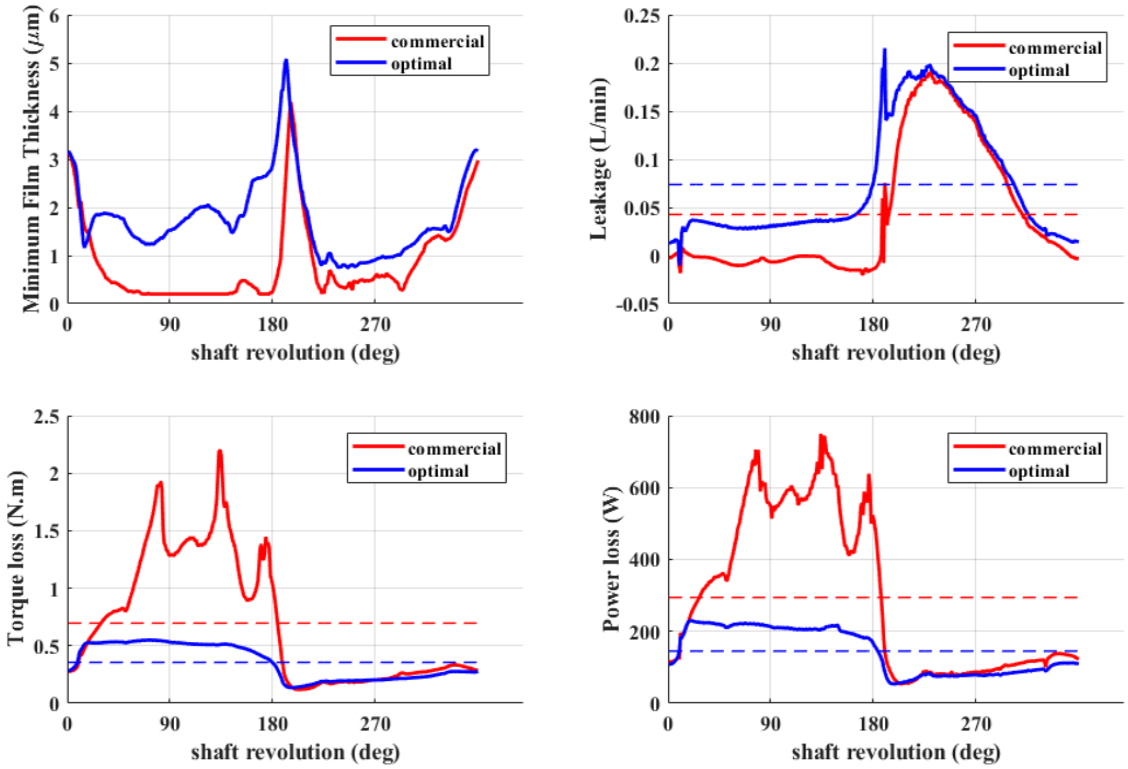

Fig. 5.15.: Comparison of performance between optimal vs commercial profile for opcon2

In opcon2, since it has high speed, the commercial profile did not fully collapse during the high pressure stroke, however during the collapsed time, viscous torque loss is larger than before due to higher speeds. Leakage for these two profiles is a bit in favor of the commercial profile and the two profiles show very similar behavior during low pressure stroke. Finally, power loss is reduced by 25% using the optimal profile which is mainly due to the difference in torque loss.

For opcon3, which is a low pressure and high speed condition, the results are shown in Figure 5.16.

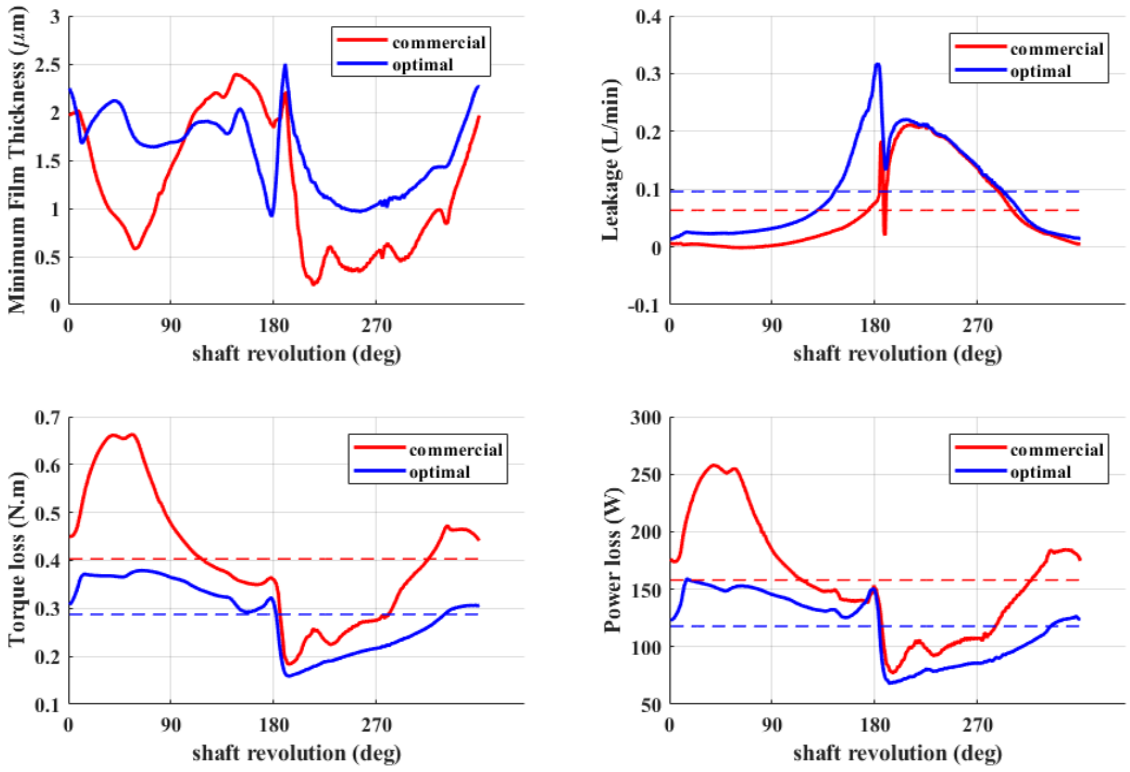

Fig. 5.16.: Comparison of performance between optimal vs commercial profile for opcon3

At first, the commercial profile shows a better minimum film thickness behavior which is above the collapse threshold but lower than the optimal profile, which also results in less leakage than the optimal case. However, the commercial case has higher torque loss due to lower film thickness values. This result suggests that the best profile needs to find the balance between leakage and torque loss. In this operating condition, due to high speed and lower pressures, torque loss is more dominant in power loss than leakage is. Finally, the optimal profile shows lower power loss due to lower torque loss for this operating condition.

In opcon4, shown in figure 5.17, film thickness values are very large for both cases and due to torque losses being very similar, leakage is the only differentiating point

between the two profiles. Power loss for the optimal profile turns out to be 18 % higher than the commercial profile.

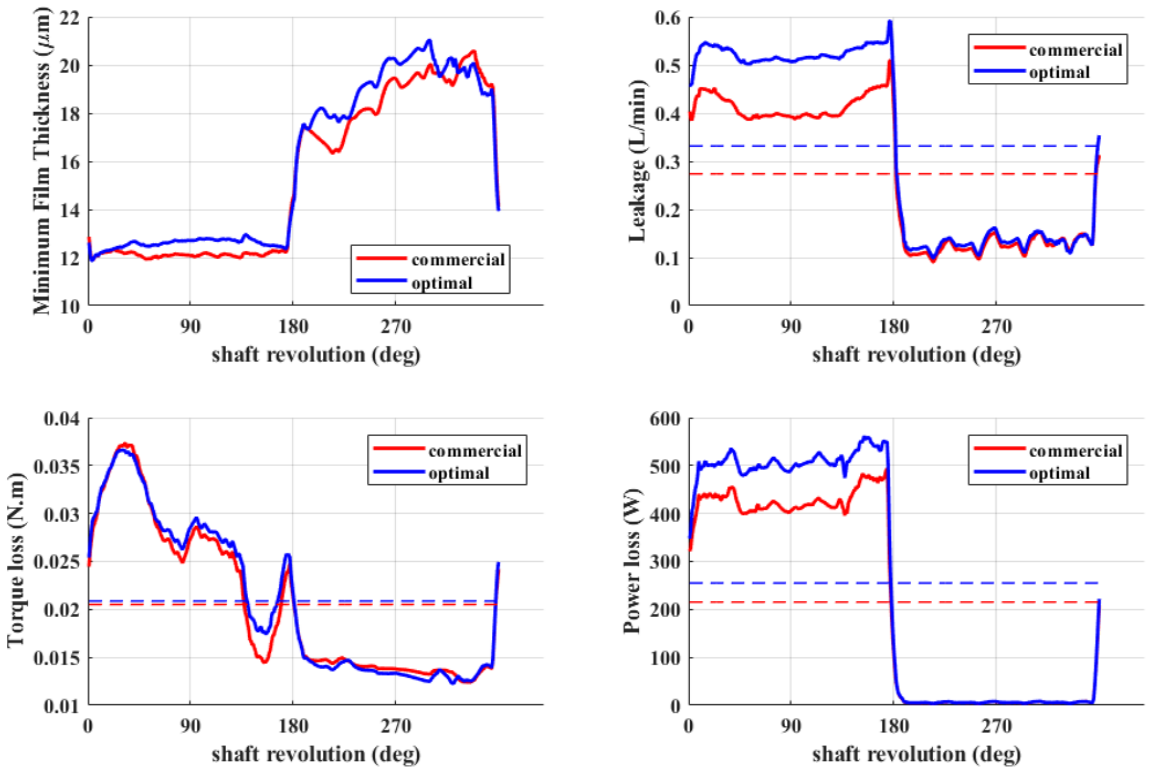

Fig. 5.17.: Comparison of performance between optimal vs commercial profile for opcon4

Opcon5 shows extensive collapse of the fluid film during the high pressure stroke for the commercial profile which leads to higher torque losses. However, leakage is very low for the commercial profile, however note that once the fluid film collapses, the shape of that profile may go through wear. Overall, for opcon5, power loss is reduced 12% when using the optimal profile. Results are shown in Figure 5.18.

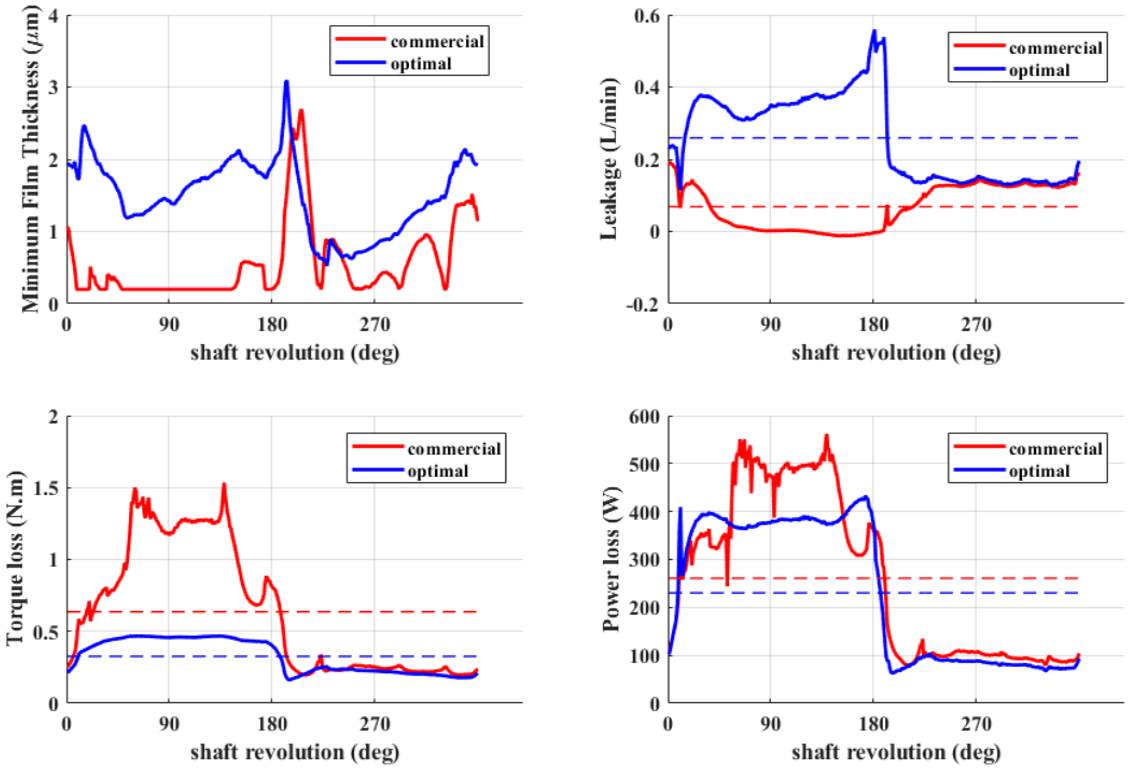

Fig. 5.18.: Comparison of performance between optimal vs commercial profile for opcon5

Moving to the last operating condition, opcon6, the optimal profile shows an improvement in performance. As shown in Figure 5.19, the leakage for the optimal case is more than double the leakage of the commercial case, however the torque loss for the commercial case is larger than the optimal case. Overall, due to the high speed and low pressure of this operating condition, power loss is reduced by 27% when using the optimal profile.

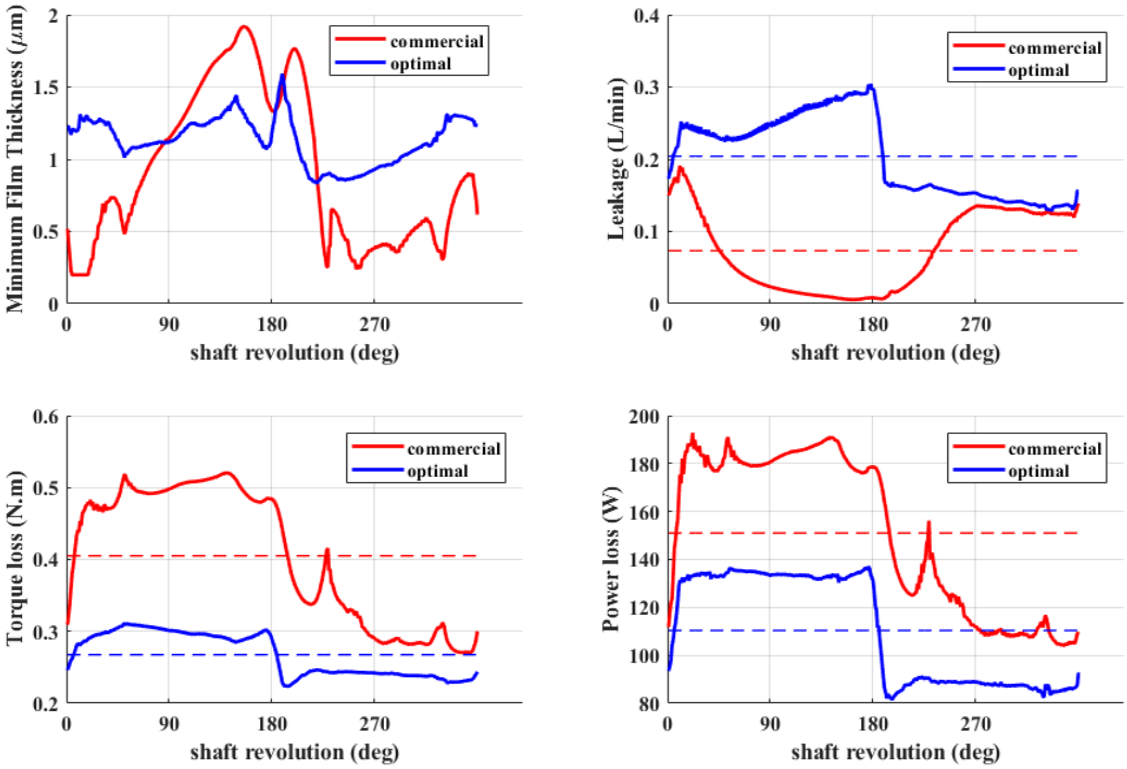

Fig. 5.19.: Comparison of performance between optimal vs commercial profile for opcon6

After looking at the results for minimum film thickness, leakage, viscous torque loss, and power loss for the two profiles, one more criteria should be looked at which is contact area ratio. Contact area ratio is the ratio of the collapsed fluid film area over the total area of the slipper sealing land averaged for each shaft angle. Figure 5.20 shows the contact area ratio for the two profiles for the six operating conditions.

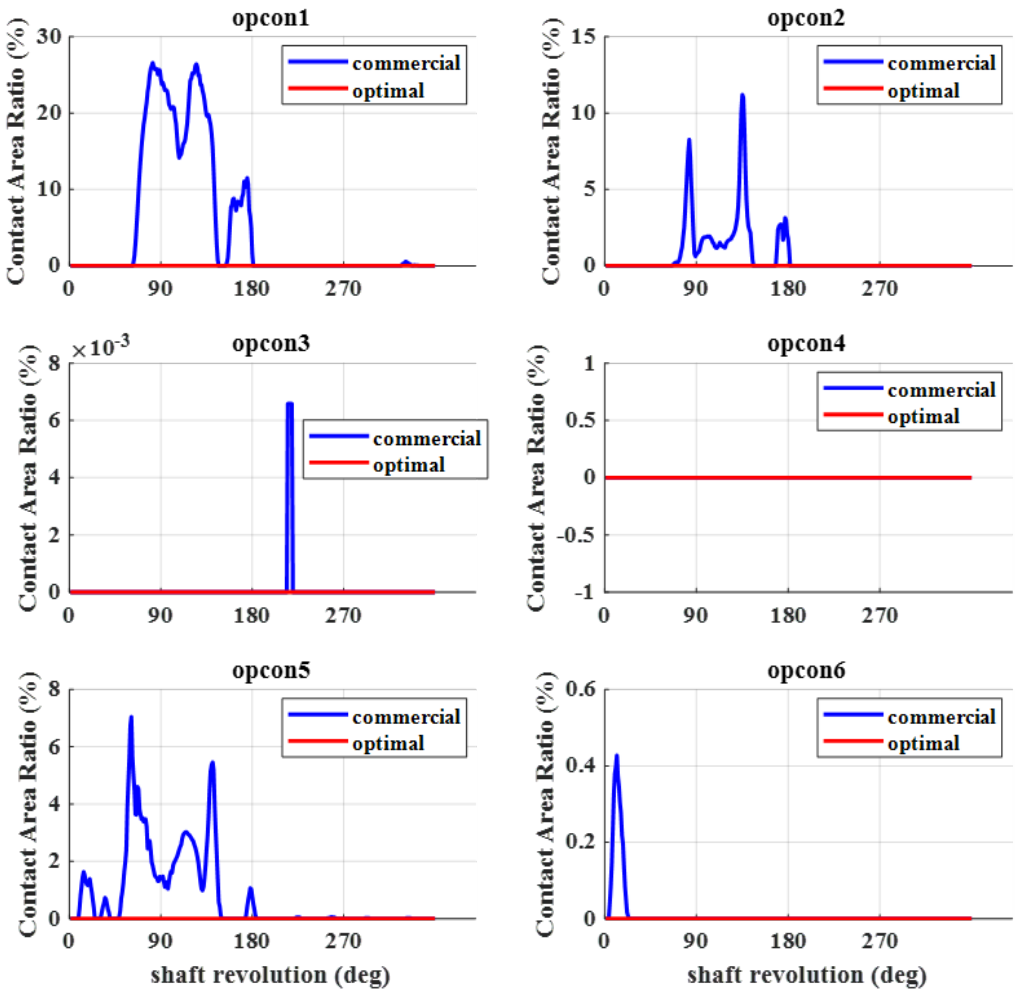

Fig. 5.20.: Contact area ratio comparison for commercial and optimal profile for all six operating conditions

The numerical values for leakage, torque loss, power loss, and contact ratio are provided in table 5.4. As it can be seen,

Table 5.4.: Comparison for commercial and optical profile

	450 bar, 600 rpm, 100% Disp.(#1)		450 bar, 3600 rpm, 100% Disp. (#2)		100 bar, 3600 rpm, 100% Disp. (#3)	
	commercial	optimal	commercial	optimal	commercial	optimal
Leakage (lpm)	0.003	0.07	0.043	0.07	0.063	0.10
Torque loss (N.m)	0.408	0.04	0.696	0.36	0.403	0.29
Power loss (W)	21.72	51.89	295.7	145.41	157.79	117.74
Contact area ratio (%)	5.0	0	0.65	0	~0	0
	450 bar, 600 rpm, 20% Disp. (#4)		450 bar, 3600 rpm, 20% Disp. (#5)		100 bar, 600 rpm, 20% Disp. (#6)	
	commercial	optimal	commercial	optimal	commercial	optimal
Leakage (lpm)	0.274	0.332	.069	0.259	.073	0.204
Torque loss (N.m)	0.021	0.021	0.636	0.326	0.405	0.268
Power loss (W)	214.42	253.9	261.87	231.3	151.35	110.5
Contact area ratio (%)	0	0	.79	0	.01	0

5.4 Conclusion

In this section, a simulation study was conducted to find an optimal macro profile for slipper surface geometry. The optimal profile removed solid to solid contact between slipper and swashplate for all operating conditions shown in table 5.3. The performance of the optimal profile was then compared to that of a commercial profile. The two profiles are shown in Figures 5.13 and 5.6. The comparison showed significant reduction in viscous torque loss for the optimal profile and an overall reduction in power loss for the optimal profile. Torque loss was reduced by 89%, 49%, 29%, 49%, and 34% respectively for opcon1, opcon2, opcon3, opcon5, and opcon6 when using the optimal profile. For opcon4, torque loss was increased by 1.7% using the optimal profile. Leakage was mainly increases when using the optimal profile. The change in power loss was +139%, -51%, -25%, +18%. -12%, and -27% for opcon1, opcon2, opcon3, opcon4, opcon5, and opcon6, respectively.

6. CONCLUSION

In this thesis, the basics of axial piston machines were introduced and the underlying principles of a fully coupled fluid-solid-thermal interaction model for slipper-swashplate interface developed by Schenk (2014) were briefly explained.

In chapter 3, the effects of swashplate vibration on the performance of the slipper-swashplate interface were analyzed. A test rig was set up and the swashplate vibration was measured at various operating conditions with speeds of 1000 and 2000 rpm, pressure difference of 100, 250, and 350 bar and maximum displacement. The vibration signal was aligned with the rotation of a certain piston to ensure the timing of the vibration signal acquired is inline with what was used in the model. The results showed that swashplate vibration for all of the operating conditions mainly affect film thickness and leakage. Film thickness and leakage values oscillate according to the pressure difference of the operating condition. The maximum amount of oscillations occur at 2000 rpm and 350 bar pressure difference. However, the overall value of leakage, torque loss, and power loss fairly remains the same for the case with and without vibration.

In chapter 4, the effects of slipper surface geometry on the behavior of the slipper-swashplate interface were studied. The surface of the slipper was expressed in a quadratic-spline equation with three variables v0,v1, and x0. v0 and v1 represent slipper surface offset at the start of sealing land and end of sealing land, and x0 represents the normalized location of sealing land at which the slipper profile has zero slope. Using an optimization scheme, with a constraint to remove solid to solid contact between slipper and swashplate, and objective of minimizing power loss, for six different operating conditions an optimal profile was obtained. The optimal profile was used in simulation for six operating conditions as shown in table 5.3 and the performance was compared with a commercial profile which was measured at Maha

facility. The results show that there is an average of 41% reduction in torque loss, an increase in leakage, and an average reduction of at least 7% in power loss when using the optimal profile.

REFERENCES

REFERENCES

J. Beale, *An Investigation of the Slipper/Swashplate Interface of Swashplate-Type Axial Piston Machines.*:Master's Thesis, Purdue University, 2017.

J. Bergada, S. Kumar, D. Davies, and J. Watton, *"A complete analysis of axial piston pump leakage and output flow ripples,"* Applied Mathematical Modeling, pp. doi:10.1016/j.apm.2011.09.016, 2011.

J. Bergada, S. Kumar, D. Davies, and J. Watton, *"A complete analysis of axial piston pump leakage and output flow ripples,"* Applied Mathematical Modeling, pp. doi:10.1016/j.apm.2011.09.016, 2011.

C. J. Hooke and Y. P. Kakoullis, *"The lubrication of slippers in axial piston pumps"* in 5th International Fluid Power Symposium, 1978.

C. J. Hooke and Y. P. Kakoullis, *"The effects of non-flatness on the performance of slippers in axial piston pumps,"* in Proc. Instn Mech. Engrs, Part C, 197C, 239-247, 1983

C. J. Hooke and Y. P. Kakoullis, *"The effects of centrifugal load and ball friction on the lubrication of slippers in axial piston pumps,"* in Proceedings of the Sixth International Symposium on Fluid power, Cambridge, paper D2, pp. 179191 (BHRA), 1981.

C. J. Hooke and K. Y. Li, *"The lubrication of overclamped slippers in axial piston pumps entrally loaded behaviour,"* in Proc. Instn Mech. Engrs, Part C, 1988, 202(C4), 287-93.

C. J. Hooke and Y. P. Kakoullis, *"On-line measurement of film thickness.,"* in Proceedings on the Conference on Instruments and computers for cost effective fluid power testing (Institution of Mechanical Engineers), 1979.

C. J. Hooke and K. Y. Li, *"The lubrication of slippers in axial piston pumps and motors - the effect of tilting couples,"* in Proc. Inst. Mech. Eng. C, 203, 1989.

C. J. Hooke and K. Y. Li, *"A note on the lubrication of composite slippers in water based axial piston pumps and motors,"* Wear, vol. 147, pp. 431-137, 1991.

C. Huang and M. Ivantysynova, *"A new approach to predict the load carrying ability of the gap between valve plate and cylinder block,"* in Bath Workshop on Power transmission and Motion Control PTMC 2003, Bath, UK, 2003.

J. Ivantysn and M. Ivantysynova, *Hydrostatic Pumps and Motor, Principles, Designs, Performance, Modeling, Analysis, Control and Testing.* New Delhi: Academic Books International, 2001.

S. Iboshi and A. Yamaguchi, *"Characteristics of a slipper bearing for swash plate type axial piston pumps and motors 1st report, theoretical analysis,"* Transactions of the Japan Society of Mechanical Engineers, Series B, vol. 48, no. 428, pp. 695-706, 1982.

S. Iboshi and A. Yamaguchi, *"Characteristics of a slipper bearing for swash plate type axial piston pumps and motors 2nd report, experiment,"* Transactions of the Japan Society of Mechanical Engineers, Series B, vol. 49, no. 437, pp. 164-171, 1983.

S. Kumar, J. Bergada, and J. Watton, *"Axial piston pump grooved slipper analysis by CFD simulation of three-dimensional NVS equation in cylindrical coordinates,"* Computers & Fluids, vol. 38, pp. 648-663, 2009.

T. Kazama and A. Yamaguchi, *"Application of a mixed lubrication model for hydrostatic thrust bearings of hydraulic equipment,"* ASME J. Tribology, vol. 115, pp. 686-691, 1993.

Manring, N.D., Johnson, R.E., Cherukuri, H.P., *"The Impact of Linear Deformation on Stationary Hydrostatic Thrust Bearing"*, ASME J. of Tribol., Vol.124, pp.874 - 877, 2002.

M. Pelosi and M. Ivantysynova, *"Heat Transfer and Thermal Elastic Deformation Analysis on the Piston/Cylinder Interface of Axial Piston Machines,"* ASME Journal of Tribology, vol. 134, pp. 1-15, 2012.

N. Shute and D. Turnbull, *"A preliminary investigation of the characteristics of hydrostatic slipper bearings,"* 1958.

N. Shute and D. Turnbull, *"A preliminary investigation into the behaviour of hydrostatic slipper pads using a 5% oil on water emulsion,"* 1964.

N. Shute and D. Turnbull, *"The losses of hydrostatic slipper bearings under various operating conditions,"* 1962.

N. Shute and D. Turnbull, *"The minimum power loss of hydrostatic slipper bearings,"* 1962.

A. Schenk, *Predicting Lubrication Performance Between the Slipper and Swashplate In Axial Piston Machines.*:Ph. D. Thesis, Purdue University, 2014.

U. Wieczorek and M. Ivantysynova, *"CASPAR - A Computer Aided Design Tool for Axial Piston Machines,"* in Proc. Bath Workshop on Power transmission and Motion Control PTMC 2000, Bath, UK, 2000, pp. 113-126.

A. Wondergem, *Piston / Cylinder Interface Of Axial Piston Machines Effect Of Piston Micro-Surface Shaping,*:Ph. D. Thesis, Purdue University, 2018.